# Synchronous Oscillations for a Coupled Cell-Bulk PDE-ODE model with Localized Cells on $\mathbb{R}^2$

Sarafa A. Iyaniwura[1], Jia Gou[2], Michael J. Ward [3]

[1] Dept. of Mathematics, University of British Columbia, Vancouver, Canada
[2] Dept. of Mathematics, University of California, Riverside, California, USA
[3] Dept. of Mathematics, University of British Columbia, Vancouver, Canada

October 13, 2020

**Abstract**

In many micro- and macro-scale systems, collective dynamics occurs from the coupling of small spatially segregated, but dynamically active, units through a bulk diffusion field. This bulk diffusion field, which is both produced and sensed by the active units, can trigger and then synchronize oscillatory dynamics associated with the individual units. In this context, we analyze diffusion-induced synchrony for a class of cell-bulk PDE-ODE system in $\mathbb{R}^2$ that has two spatially segregated dynamically active circular cells of small radius. By using strong localized perturbation theory in the limit of small cell radius, we calculate the steady-state solution and formulate the linear stability problem. For Sel'kov intracellular reaction kinetics, we analyze how the effect of bulk diffusion can trigger, via a Hopf bifurcation, either in-phase or anti-phase intracellular oscillations that would otherwise not occur for cells that are uncoupled from the bulk medium. Phase diagrams in parameter space where these oscillations occur are presented, and the theoretical results from the linear stability theory are validated from full numerical simulations of the PDE-ODE system. In addition, the two-cell case is extended to study the onset of synchronous oscillatory instabilities associated with an infinite hexagonal arrangement of small identical cells in $\mathbb{R}^2$ with Sel'kov intracellular kinetics. This analysis for the hexagonal cell pattern relies on determining a new, computationally efficient, explicit formula for the regular part of a certain periodic reduced-wave Green's function.

**Key words:** Hopf bifurcation, synchronous oscillations, cell-bulk coupling, Green's function.

## 1 Introduction

In many micro- and macro-scale systems, such as those in microbial intracellular communication and in chemo-physical systems involving catalyst particles, collective dynamics occurs from the coupling of small, spatially segregated, but dynamically active, "units" through a bulk diffusion field. This bulk diffusion field, which is both produced and sensed by the active units, can both trigger and then synchronize oscillatory dynamics associated with the individual units. There is an extensive ODE-based theory for the synchronization of oscillations associated with dynamically active units as a result of a wide-variety of coupling mechanisms (see [27] for a survey). However, in many applications the coupling of dynamically active units is more appropriately modeled by a PDE diffusion field. In this context, in this paper we analyze diffusion-induced synchrony for a class of PDE-ODE system in $\mathbb{R}^2$ that has two spatially segregated dynamically active circular cells of small radius. Extensions of the two-cell theory to treat an infinite hexagonal arrangement of cells is given.

We begin by formulating the coupled cell-bulk PDE-ODE system for two identical cells in $\mathbb{R}^2$, as motivated by [24] and extended in [14] and [19]. In the bulk region, the diffusion field $\mathcal{U}(\boldsymbol{X}, T)$ is assumed to satisfy

$$\frac{\partial \mathcal{U}}{\partial T} = D_B \,\Delta \mathcal{U} - k_B \,\mathcal{U}\,, \qquad T > 0\,, \quad \boldsymbol{X} \in \mathbb{R}^2 \setminus \cup_{j=1}^{2} \Omega_j\,; \tag{1.1a}$$

$$D_B \,\partial_{n_{\boldsymbol{X}}} \mathcal{U} = \beta_1 \,\mathcal{U} - \beta_2 \,\mu_j^1\,, \qquad \boldsymbol{X} \in \partial\Omega_j\,, \quad j = 1, 2\,. \tag{1.1b}$$

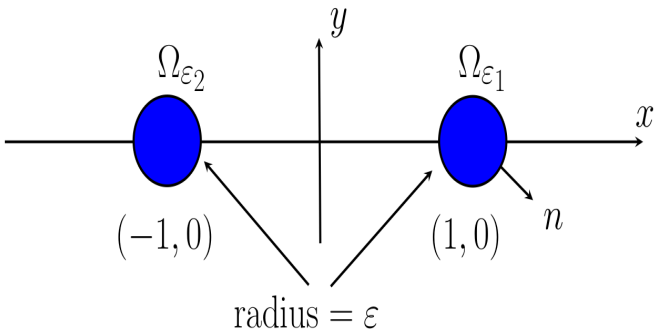


*Figure 1: Schematic plot of the geometry of two cells on the infinite plane centered at* $(\pm 1, 0)$ *in non-dimensional variables.*

Here $D_B > 0$ and $k_B > 0$ are the dimensional diffusion coefficient and rate of degradation of chemical in the bulk region, respectively, $\beta_1 > 0$ and $\beta_2 > 0$ are common dimensional influx and efflux parameters into and out of the two cells, and $\partial_{n_{\boldsymbol{X}}}$ denotes the outer normal derivative of the $j^{\text{th}}$ cell $\Omega_j$ pointing into the bulk region. The signaling compartments $\Omega_j$ for $j = 1, 2$ are assumed to be disks of a common radius $R_0$ centered at $\boldsymbol{X}_j \in \mathbb{R}^2$ for $j = 1, 2$. We suppose there are $n$ interacting chemical species in each cell represented by the vector $\boldsymbol{\mu}_j \equiv (\mu_j^1, \ldots, \mu_j^n)^T$ for the $j^{\text{th}}$ cell. Then, the extracellular bulk dynamics (1.1) is coupled to the $n$-dimensional system of ODEs for the common intracellular kinetics $\boldsymbol{F}$ within the $j^{\text{th}}$ cell through an integration of the diffusive flux across the cell membrane, as

$$\frac{\mathrm{d}\boldsymbol{\mu}_j}{\mathrm{d}T} = k_R \mu_c \boldsymbol{F}\left(\boldsymbol{\mu}_j/\mu_c\right) + \boldsymbol{e}_1 \int_{\partial\Omega_j} \left(\beta_1 \mathcal{U} - \beta_2\, \mu_j^1\right) \mathrm{d}S_{\boldsymbol{X}}\,, \qquad j = 1, 2\,. \tag{1.1c}$$

Here $\boldsymbol{e}_1 \equiv (1, 0, \ldots, 0)^T \in \mathbb{R}^n$, $k_R > 0$ is the dimensional reaction rate, and $\mu_c > 0$ is a typical value for $\boldsymbol{\mu}_j$. In this cell-bulk PDE-ODE model (1.1) it is assumed that the cell membrane is only permeable to one signaling chemical, labeled by $\mu_j^1$, as controlled by the efflux parameter $\beta_2$. This signaling molecule generated by one cell communicates with the other cell through diffusion in the bulk medium. The influx permeability parameter $\beta_1$ controls the global feedback into the two cells from the bulk diffusion field generated by both cells.

Without loss of generality, we can assume that the cells are centered at $(\pm L, 0)$ on the infinite plane. By using the half-distance $L$ between the cell centers as the length-scale, we non-dimensionalize (1.1) as

$$t = k_R T\,, \qquad \boldsymbol{x} = \frac{\boldsymbol{X}}{L}\,, \qquad U = \frac{L^2}{\mu_c}\mathcal{U}\,, \qquad \boldsymbol{u} = \frac{\boldsymbol{\mu}}{\mu_c}\,, \tag{1.2}$$

and assume that $\varepsilon \equiv R_0/L \ll 1$. Our assumption that $\varepsilon \ll 1$ implies that the two cells are well-separated, in the sense that the inter-cell distance is much larger than the cell radius. In terms of (1.2), (1.1) becomes

$$\begin{aligned} &\tau\, U_t = D\Delta U - U\,, \qquad t > 0\,, \quad \boldsymbol{x} \in \mathbb{R}^2 \setminus \cup_{j=1}^2 \Omega_{\varepsilon_j}\,; \\ &\varepsilon\, D\, \partial_n U = d_1\, U - d_2\, u_j^1\,, \qquad \boldsymbol{x} \in \partial\Omega_{\varepsilon_j}\,, \quad j = 1, 2\,, \end{aligned} \tag{1.3a}$$

in the bulk region, where $\Omega_{\varepsilon_j} \equiv \{\boldsymbol{x}\,|\,|\boldsymbol{x} - \boldsymbol{x}_j| \le \varepsilon\}$, $\boldsymbol{x}_1 \equiv (1, 0)^T$, and $\boldsymbol{x}_2 \equiv (-1, 0)^T$ (see Fig. 1 for a schematic). This PDE is coupled to the common intracellular dynamics within the two cells by

$$\frac{\mathrm{d}\boldsymbol{u}_j}{\mathrm{d}t} = \boldsymbol{F}(\boldsymbol{u}_j) + \frac{\boldsymbol{e}_1}{\varepsilon\,\tau} \int_{\partial\Omega_{\varepsilon_j}} \left(d_1\, U - d_2\, u_j^1\right)\, \mathrm{d}S_{\boldsymbol{x}}\,, \qquad j = 1, 2\,. \tag{1.3b}$$

The dimensionless parameters in (1.3) are

$$\tau \equiv \frac{k_R}{k_B}\,, \qquad D \equiv \frac{D_B}{L^2\, k_B}\,, \qquad d_1 \equiv \frac{\varepsilon\,\beta_1}{L\, k_B} = \mathcal{O}(1)\,, \qquad d_2 \equiv \frac{\varepsilon\,\beta_2 L}{k_B} = \mathcal{O}(1)\,. \tag{1.4}$$

To ensure that there is $\mathcal{O}(1)$ transport across the cell boundaries we assumed in (1.4) that $\beta_1$ and $\beta_2$ are both $\mathcal{O}(\varepsilon^{-1})$. The key non-dimensional parameters in (1.3) are the reaction-time parameter $\tau$, the effective diffusivity $D$, and the permeabilities $d_1$ and $d_2$. We observe that larger values of $D$ correspond to smaller values of $L$, where the cells are more closely spaced. For small values of $\tau$, the time-scale for the bulk decay of the signaling molecule is much faster than the rate of the intracellular reactions. As a result, there is only a weak cell-cell interaction when $\tau$ is small.

Cell-bulk PDE-ODE models of the form (1.1) provide a relatively new modeling framework for analyzing how a passive bulk diffusion field mediates collective dynamical behavior associated with spatially segregated, but dynamically active, immobile reaction sites of small area. This modeling framework applies to certain microbial systems, such as collections of yeast cells or social amoeba, where the diffusion of an extracellular signaling molecule, referred to as an autoinducer, is known to trigger synchronized intracellular oscillations (cf. [8], [15], [9], [10], [12], [32], [22]). By modifying (1.1c) slightly to allow for surface reactions on a collection of small cells, instead of intracellular reactions, the framework (1.1) is also relevant for the macro-scale problem of studying synchronous chemical oscillations of a collection of small chemically-coated catalyst particles immersed in a BZ chemical mixture (cf. [28], [30], [29]). In a related macro-scale context, the framework (1.1) is relevant for characterizing the global dynamical behavior of heterogeneous catalytic systems that depends on the communication of spatially localized reaction sites through diffusion in the gas-phase above the reactive surface (cf. [36]).

Our analysis of the triggering of intracellular oscillations mediated by the bulk diffusion field for the cell-bulk PDE-ODE model (1.3) on the infinite domain is an extension of that given in [14] and [19]) for a finite disk-shaped domain, and is motivated by observations in [22], [32], and [12] for microbial systems. In particular, the experimental study of [22] showed that it is more difficult to trigger collective dynamics for cells in open domains with no boundaries than in finite-domain systems, owing to the reduction in the autoinducer signal as it can diffuse away from the cells and off to infinity in the unbounded domain. In [32] it was shown that with absorbing, rather than reflecting, boundaries on a finite domain the autoinducer level near the cells can decrease by a large factor, which thereby precludes the possibility of collective dynamics. Finally, the benefit of a more spatially clustered arrangement of cells for triggering collective oscillations was emphasized in [12].

The outline of this paper is as follows: In §2 we use the method of matched asymptotic expansions in the limit $\varepsilon \to 0$ of small cell radius to formulate the steady-state problem for (1.3) and to derive the corresponding linear stability problem for the linearization of the steady-state. For the specific choice of Sel'kov intracellular reaction kinetics, in §2.2 we show that there is a unique steady-state solution for (1.3). In addition, we derive nonlinear scalar transcendental equations for the discrete eigenvalues of the linearization of this unique steady-state for both in-phase and anti-phase instabilities of the two-cells. In §3 we provide phase diagrams in the $\tau$ versus $D$ parameter space where either in-phase or anti-phase intracellular oscillations are triggered due to the bulk coupling. In contrast to two cells in a disk-shaped domain (cf. [14], [19]), there is a large parameter regime where anti-phase oscillations can occur. Detailed spectral results, as obtained by taking a slice through the phase diagram, show that mixed-mode intracellular oscillations can occur. The linear stability theory is confirmed through full PDE simulations of (1.3) using FlexPDE [11]. From an alternative non-dimemsionalization of (1.3), in §3.1 we show that anti-phase oscillations are only possible if the inter-cell separation distance exceeds a threshold. In §4 we formulate the steady-state and linear stability problem for the cell-bulk PDE-ODE model with Sel'kov kinetics for a hexagonal arrangement of identical cells in $\mathbb{R}^2$. The implementation of the steady-state and linear stability theory is based on the derivation in Appendix A of an explicit, and computationally efficient, formula for the regular part of a reduced wave-Green's function with either periodic or Floquet boundary conditions on the boundary of the fundamental Wigner Seitz cell for the hexagonal lattice. Periodic or Floquet Helmholtz Green's functions commonly arise in acoustic or electromagnetic wave scattering problems involving periodic arrangements of small scattering bodies (cf. [21], [23]). Our derivation in Appendix A for the reduced-wave Green's function is an extension of the analysis in [6] and [17]. Finally, in §5 we briefly discuss two open problems for diffusion-mediated communication.

## 2 Two Cells: Steady-States, Linear Stability, and Sel'kov Kinetics

In this section we formulate the steady-state and linear stability problems for (1.3) by adapting the singular perturbation analysis in [19] and [13] to the infinite-plane problem. We then apply the theory to the case of Sel'kov intracellular reaction kinetics in order to obtain phase diagrams in parameter space where intracellular oscillations

are triggered by the cell-cell coupling through the bulk diffusion field.

## 2.1 Steady-state and linear stability analysis

In the limit $\varepsilon \to 0$, the steady-state solution to (1.3) can be constructed using strong localized perturbation theory (cf. [34], [35]). Since a similar analysis was done in [19] and [13] for the finite-domain problem, we only give a brief sketch of the derivation here.

In the $j^{\text{th}}$ inner region, defined within an $\mathcal{O}(\varepsilon)$ neighborhood of the $j^{\text{th}}$ cell boundary, we introduce the local variables $\boldsymbol{y} = \varepsilon^{-1}(\boldsymbol{x} - \boldsymbol{x}_j)$ and $U_j(\boldsymbol{x}) = U_j(\varepsilon \boldsymbol{y} + \boldsymbol{x}_j)$, with $\rho \equiv |\boldsymbol{y}|$. From (1.3), we obtain that the leading order steady-state problem near the $j^{\text{th}}$ cell, for $j = 1, 2$, is

$$\Delta U_j = 0\,, \quad \rho \geq 1\,; \qquad D\partial_\rho U_j = d_1 U_j - d_2 u_j^1\,, \quad \rho = 1\,. \tag{2.1}$$

This problem has the radially symmetric solution

$$U_j(\rho) = A_j \log \rho + \frac{1}{d_1}\left(D\, A_j + d_2 u_j^1\right)\,, \qquad j = 1, 2\,, \tag{2.2}$$

where $A_j$ for $j = 1, 2$ are constants to be determined. By using (2.2) in the ODE system (1.3b) for the intracellular dynamics, we conclude that its steady-state solution must satisfy

$$\boldsymbol{F}\left(\boldsymbol{u}_j\right) + \frac{2\pi D}{\tau}\, A_j \boldsymbol{e}_1 = \boldsymbol{0}\,, \qquad j = 1, 2\,. \tag{2.3}$$

This determines $\boldsymbol{u}_j$ in terms of the unknown constant $A_j$. A further equation is obtained below by matching the far-field behavior of the inner solution (2.2) to the steady-state solution in the outer bulk region.

From an asymptotic matching of the far-field of the inner solution (2.2) to an outer steady-state solution for (1.3a), we obtain that the leading order outer bulk solution, labeled by $U$, must satisfy

$$\begin{aligned} &\Delta U - \frac{1}{D}\, U = 0\,, \quad \boldsymbol{x} \in \mathbb{R}^2 \setminus \{\boldsymbol{x}_1, \boldsymbol{x}_2\}\,; \\ &U \sim A_j \log|\boldsymbol{x} - \boldsymbol{x}_j| + \frac{A_j}{\nu} + \frac{1}{d_1}(D A_j + d_2 u_j^1)\,, \quad \text{as} \quad \boldsymbol{x} \to \boldsymbol{x}_j\,, \quad j = 1, 2\,, \end{aligned} \tag{2.4}$$

where $\nu \equiv -1/\log\varepsilon$. From (2.4) we observe that the pre-specification of the precise form of the regular part of the singularity as $\boldsymbol{x} \to \boldsymbol{x}_j$ for $j = 1, 2$ will provide the extra conditions relating $\boldsymbol{u}_j$ to $A_j$.

The solution to (2.4) is represented as

$$U = -2\pi \sum_{i=1}^{2} A_i G(\boldsymbol{x}; \boldsymbol{x}_i)\,, \tag{2.5}$$

where $G(\boldsymbol{x}; \boldsymbol{x}_j)$ is the free-space Green's function satisfying

$$\Delta G - \frac{1}{D} G = -\delta(\boldsymbol{x} - \boldsymbol{x}_j)\,, \quad \boldsymbol{x} \in \mathbb{R}^2\,, \tag{2.6}$$

which is given explicitly, in terms of the modified Bessel function of the second kind of order zero, by

$$G(\boldsymbol{x}; \boldsymbol{x}_j) = \frac{1}{2\pi} K_0\left(|\boldsymbol{x} - \boldsymbol{x}_j|/\sqrt{D}\right)\,. \tag{2.7a}$$

As $\boldsymbol{x} \to \boldsymbol{x}_j$, by using the small argument asymptotics of $K_0(z)$ (cf. [2]), the regular part $R$ of the singularity is

$$G(\boldsymbol{x}, \boldsymbol{x}_j) \sim \frac{1}{2\pi} \log|\boldsymbol{x} - \boldsymbol{x}_j| + R + o(1)\,, \quad \text{as} \quad \boldsymbol{x} \to \boldsymbol{x}_j\,; \qquad R \equiv \frac{1}{2\pi}\left(\log 2 - \gamma_e + \frac{1}{2}\log D\right)\,, \tag{2.7b}$$

where $\gamma_e$ is Euler's constant.

Next, we expand (2.5) as $\boldsymbol{x} \to \boldsymbol{x}_j$ and enforce that the resulting expression agrees with the prescribed singularity behavior in (2.4). In this way, we obtain the following nonlinear algebraic system (NAS) for the vector $\mathcal{A} \equiv (A_1, A_2)^T$:

$$\left( \left(1 + \frac{\nu D}{d_1}\right) I + 2\pi\nu\mathcal{G} \right)\boldsymbol{\mathcal{A}} = -\frac{\nu d_2}{d_1}\,\boldsymbol{u}^1\,, \qquad \boldsymbol{F}\,(\boldsymbol{u}_j) + \frac{2\pi D}{\tau}\,A_j \boldsymbol{e}_1 = \boldsymbol{0}\,, \quad j = 1,2\,; \qquad \mathcal{G} \equiv \begin{pmatrix} R & G_{12} \\ G_{21} & R \end{pmatrix}. \tag{2.8}$$

In (2.8), the entries of the Green's matrix $\mathcal{G}$ are given by $G_{12} = G_{21} = G(\boldsymbol{x}_1;\boldsymbol{x}_2) = (2\pi)^{-1}K_0\left(2/\sqrt{D}\right)$, and $R$ is defined in (2.7b). Moreover, in (2.8), the vector $\boldsymbol{u}^1 \equiv (u_1^1, u_2^1)^T$ is the steady-state for the signaling molecule that is secreted into the bulk region by the two cells.

Next, we formulate the linear stability problem. We suppose that the NAS (2.8) has a solution, which yields an approximation to the steady-state solution $U_e(x)$ and $\boldsymbol{u}_{ej}$ to (1.3). To determine the linear stability of this steady-state we introduce the perturbation

$$U(\boldsymbol{x},t) = U_e(\boldsymbol{x}) + e^{\lambda t}\xi(\boldsymbol{x}) \qquad \text{and} \qquad \boldsymbol{u}_j(t) = \boldsymbol{u}_{ej} + e^{\lambda t}\boldsymbol{\phi}_j\,, \qquad j = 1,2\,, \tag{2.9}$$

into (1.3) where $\boldsymbol{\phi}_j \equiv (\phi_j^1, \ldots, \phi_j^n)^T$. Upon linearizing (1.3), we obtain that

$$\tau\lambda\xi = D\,\Delta\xi - \xi\,, \quad \boldsymbol{x} \in \mathbb{R}^2 \setminus \cup_{j=1}^2 \Omega_{\varepsilon_j}\,; \qquad \varepsilon D\,\partial_{nj}\xi = d_1\,\xi - d_2\,\phi_j^1\,, \quad \boldsymbol{x} \in \partial\Omega_{\varepsilon_j}\,, \quad j = 1,2\,, \tag{2.10a}$$

which is coupled to the linearized intracellular dynamics within the two cells by

$$\lambda\boldsymbol{\phi}_j = J_j\,\boldsymbol{\phi}_j + \frac{\boldsymbol{e}_1}{\varepsilon\tau}\int_{\partial\Omega_{\varepsilon_j}} (d_1\,\xi - d_2\,\phi_j^1)\,\mathrm{d}s\,, \qquad j = 1,2\,. \tag{2.10b}$$

Here $J_j \equiv J(\boldsymbol{u}_{ej})$ is the Jacobian matrix of the local kinetics $\boldsymbol{F}$ evaluated at the steady-state $\boldsymbol{u}_{ej}$.

We now use strong localized perturbation theory on (2.10) to derive, similar to the analysis in [19] for the finite-domain case, a nonlinear matrix eigenvalue problem, referred to as the globally coupled eigenvalue problem (GCEP), that determines asymptotic approximations as $\varepsilon \to 0$ for the discrete eigenvalues $\lambda$ of the linearization (2.10).

In the inner region, defined within an $\mathcal{O}(\varepsilon)$ neighborhood of the $j^{\text{th}}$ cell, we introduce the local variables $\boldsymbol{y} = \varepsilon^{-1}(\boldsymbol{x} - \boldsymbol{x}_j)$ and $\xi_j(\boldsymbol{x}) \equiv \xi_j(\boldsymbol{x}_j + \varepsilon\boldsymbol{y})$ with $\rho = |\boldsymbol{y}|$. For $\varepsilon \to 0$, we obtain from (2.10) that

$$\Delta\,\xi_j = 0\,, \quad 1 < \rho < \infty\,; \qquad D\,\partial_\rho\,\xi_j = d_1\xi_j - d_2\phi_j^1\,, \quad \text{on} \quad \rho = 1\,, \tag{2.11}$$

in the $j^{\text{th}}$ inner region, where $j = 1, 2$. The radially symmetric solution to (2.11) is

$$\xi_j = c_j \log\rho + \frac{1}{d_1}\left(D\,c_j + d_2\phi_j^1\right)\,, \qquad j = 1,2\,, \tag{2.12}$$

where the constants $c_j$, for $j = 1, 2$, are to be found. We then substitute (2.12) into the linearized intracellular dynamics (2.10b) to obtain that

$$(J_j - \lambda I)\boldsymbol{\phi}_j = -\frac{2\pi D}{\tau}\,c_j\boldsymbol{e}_1\,. \qquad j = 1,2\,. \tag{2.13}$$

As needed below, we must calculate $\boldsymbol{\phi}^1 \equiv (\phi_1^1, \phi_2^1)^T$ from (2.13). We readily find that

$$\boldsymbol{\phi}^1 = \frac{2\pi D}{\tau}\mathcal{K}\boldsymbol{c}\,, \tag{2.14}$$

where $\boldsymbol{c} \equiv (c_1, c_2)^T$ and the diagonal matrix $\mathcal{K}$ is defined by

$$\mathcal{K} \equiv \mathrm{diag}\,(K_1, K_2)\,, \qquad K_j = \boldsymbol{e}_1^T(\lambda I - J_j)^{-1}\boldsymbol{e}_1 = \frac{\boldsymbol{e}_1^T N_j \boldsymbol{e}_1}{\det(\lambda I - J_j)} = \frac{(N_j)_{11}}{\det(\lambda I - J_j)}\,. \tag{2.15}$$

Here $(N_j)_{11}$ is the entry in the first column and first row of the $n \times n$ matrix $N_j$ of cofactors of $(\lambda I - J_j)$.

Next, we analyze the bulk solution for (2.10) in the outer region. By matching the far-field behaviour of the inner solution (2.12) to the outer solution we obtain a specific singularity behaviour for the outer solution as $\boldsymbol{x} \to \boldsymbol{x}_j$. In this way, the outer solution for (2.10) in the bulk region satisfies

$$\begin{aligned} &\Delta\xi - \frac{(1+\tau\lambda)}{D}\,\xi = 0\,, \quad \boldsymbol{x} \in \mathbb{R}^2 \setminus \{\boldsymbol{x}_1, \boldsymbol{x}_2\}\,; \\ &\xi \sim c_j \log|\boldsymbol{x}-\boldsymbol{x}_j| + \frac{c_j}{\nu} + \frac{1}{d_1}(Dc_j + d_2\phi_j^1)\,, \quad \text{as} \quad \boldsymbol{x} \to \boldsymbol{x}_j\,, \qquad j = 1,2\,, \end{aligned} \tag{2.16}$$

where $\nu \equiv -1/\log\varepsilon$. The solution to (2.16) is represented as

$$\xi(\boldsymbol{x}) = -2\pi \sum_{i=1}^{2} c_i\, G_\lambda(\boldsymbol{x};\boldsymbol{x}_i)\,, \tag{2.17}$$

where $G_\lambda(\boldsymbol{x};\boldsymbol{x}_j)$ is the free-space Green's function for $\Delta G_\lambda - D^{-1}(1+\tau\lambda)G_\lambda = -\delta(\boldsymbol{x}-\boldsymbol{x}_j)$ in $\mathbb{R}^2$, with regular part $R_\lambda$, which is identified from the local behavior $G_\lambda(\boldsymbol{x};\boldsymbol{x}_j) \sim -(2\pi)^{-1}\log|\boldsymbol{x}-\boldsymbol{x}_j| + R_\lambda + o(1)$ for $\boldsymbol{x} \to \boldsymbol{x}_j$ as

$$G_\lambda(\boldsymbol{x};\boldsymbol{x}_j) = \frac{1}{2\pi}K_0\left(\sqrt{\frac{1+\tau\lambda}{D}}|\boldsymbol{x}-\boldsymbol{x}_j|\right)\,, \qquad R_\lambda \equiv \frac{1}{2\pi}\left[\log 2 - \gamma_e - \frac{1}{2}\log\left(\frac{1+\tau\lambda}{D}\right)\right]\,. \tag{2.18}$$

Here the principal branch of $\sqrt{(1+\tau\lambda)/D}$ is chosen to ensure that $G_\lambda$ is analytic in $\mathrm{Re}(\lambda) > 0$ and that $G_\lambda$ decays exponentially as $|\boldsymbol{x}| \to \infty$.

Next, we expand (2.17) as $\boldsymbol{x} \to \boldsymbol{x}_j$ and enforce that the non-singular terms in the resulting expression agree with those specified in (2.16) for $j = 1, 2$. This yields a linear system for $\boldsymbol{c} \equiv (c_1, c_2)^T$ of the form

$$\left(I + 2\pi\nu\mathcal{G}_\lambda + \frac{\nu D}{d_1}I\right)\boldsymbol{c} = -\frac{\nu d_2}{d_1}\boldsymbol{\phi}^1\,, \tag{2.19}$$

where $\boldsymbol{\phi}^1$ is given in (2.14). Finally, by substituting (2.14) into (2.19), we obtain a $2\times 2$ homogeneous linear system for $\boldsymbol{c}$

$$\mathcal{M}(\lambda)\boldsymbol{c} = \boldsymbol{0}\,, \qquad \text{where} \qquad \mathcal{M}(\lambda) \equiv \left(1 + \frac{\nu D}{d_1}\right)I + 2\pi\nu\mathcal{G}_\lambda + \frac{2\pi\nu D d_2}{\tau d_1}\mathcal{K}\,, \qquad \mathcal{G}_\lambda \equiv \begin{pmatrix} R_\lambda & G_{\lambda 12} \\ G_{\lambda 21} & R_\lambda \end{pmatrix}\,, \tag{2.20a}$$

where the diagonal matrix $\mathcal{K} = \mathcal{K}(\lambda)$ was defined in (2.15). In the symmetric eigenvalue-dependent Green's matrix $\mathcal{G}_\lambda$, where we defined $G_{\lambda 12} = G_{\lambda 21} \equiv G_\lambda(\boldsymbol{x}_1;\boldsymbol{x}_2)$, we have from (2.18) that

$$G_{\lambda 12} = \frac{1}{2\pi}K_0\left(2\sqrt{\frac{1+\tau\lambda}{D}}\right)\,, \qquad R_\lambda \equiv \frac{1}{2\pi}\left[\log 2 - \gamma_e - \frac{1}{2}\log\left(\frac{1+\tau\lambda}{D}\right)\right]\,. \tag{2.20b}$$

The GCEP (2.20) is a nonlinear matrix eigenvalue problem for $\lambda$, which has a nontrivial solution $\boldsymbol{c} \neq \boldsymbol{0}$ if and only if $\lambda$ satisfies $\det\mathcal{M}(\lambda) = 0$. In this way, for $\varepsilon \to 0$, the discrete eigenvalues of the linearization (2.10) are approximated by the set $\Lambda(\mathcal{M})$ of all such roots, as defined by

$$\Lambda(\mathcal{M}) \equiv \{\lambda \,|\, \det\mathcal{M}(\lambda) = 0\}\,. \tag{2.21}$$

Nonlinear matrix eigenvalue problems for certain classes of matrices, and computational techniques to solve them, are surveyed in [16] and [5]. For a broad range of applications, as discussed in [4], the corresponding matrix $\mathcal{M}(\lambda)$ is either a polynomial or rational function of $\lambda$. In our context, although $\mathcal{M}(\lambda)$ is only a $2\times 2$ matrix, this matrix is highly nonlinear in $\lambda$ owing to its dependence on the eigenvalue-dependent Green's matrix $\mathcal{G}_\lambda$ as well as on $\mathcal{K}(\lambda)$.

In terms of the eigenvectors $\boldsymbol{c}$ and eigenvalues $\lambda \in \Lambda(\mathcal{M})$ of the GCEP (2.20), the linearization around the steady-state bulk solution and the secretable steady-state intracellular component is, for $\varepsilon \to 0$, given by the superposition

$$U(\boldsymbol{x},t) \sim U_e - \sum_{\lambda\in\Lambda(\mathcal{M})} e^{\lambda t}\left(\sum_{j=1}^{2} c_j G_\lambda(\boldsymbol{x};\boldsymbol{x}_j)\right)\,; \qquad u_j^1 \sim u_{ej}^1 + \frac{2\pi D}{\tau}\sum_{\lambda\in\Lambda(\mathcal{M})}(\mathcal{K}\boldsymbol{c})_j\, e^{\lambda t}\,, \qquad j = 1,2\,, \tag{2.22}$$

where each $\boldsymbol{c} = (c_1, c_2)^T$ depends on the particular eigenvalue $\lambda$. From (2.22), the vector $\mathcal{K}\boldsymbol{c}$ provides amplitude and phase information for small-amplitude intracellular oscillations within the two cells at a Hopf bifurcation point as characterized by $\det \mathcal{M}(i\lambda_I) = 0$ with $\lambda_I > 0$, where $\lambda = i\lambda_I \in \Lambda(\mathcal{M})$ is the eigenvalue with the largest real part.

## 2.2 Sel'kov reaction kinetics

We now illustrate the steady-state and linear stability theory for the two-component, i.e. $(n = 2)$, Sel'kov reaction-kinetics [26], defined in terms of $\boldsymbol{u}_j = (v_j, w_j)^T$ and $\boldsymbol{F}(v_j, w_j) = (F_1(v_j, w_j), F_2(v_j, w_j))^T$ by

$$F_1(v_j, w_j) = \alpha w_j + w_j v_j^2 - v_j\,, \qquad F_2(v_j, w_j) = \zeta\left[\mu - \left(\alpha w_j + w_j v_j^2\right)\right]\,. \tag{2.23}$$

Here the Sel'kov kinetic parameters $\alpha > 0$, $\mu > 0$ and $\zeta > 0$ are common to both cells.

When there is no influx (i.e. $d_1 = 0$), the two cells are uncoupled from the bulk medium, and (1.3b) reduces to the conventional ODE dynamics

$$\frac{\mathrm{d}\boldsymbol{u}_j}{\mathrm{d}t} = \boldsymbol{F}\left(\boldsymbol{u}_j\right) - \frac{2\pi d_2 v_j}{\tau}\boldsymbol{e}_1\,, \tag{2.24}$$

where $\boldsymbol{F}$ is defined in (2.23). From a standard ODE analysis based on calculating the Jacobian and determinant of the unique steady-state for (2.24), it is readily shown that this steady state is linearly stable only when

$$\alpha > \alpha_c \equiv -\frac{\mu^2}{\chi^2} + \frac{1}{2\zeta}\left[-\chi + \sqrt{\chi^2 + \frac{8\zeta\mu^2}{\chi}}\right]\,, \quad \text{where} \quad \chi \equiv 1 + \frac{2\pi d_2}{\tau}\,. \tag{2.25}$$

Then, by using the Poincare-Bendixson theorem, it follows that (2.24) will have periodic limit cycle oscillations on the range $0 < \alpha < \alpha_c$ where the unique steady-state for (2.24) is unstable. With $d_2 = 0$, corresponding to the case where there is no efflux from the cell, the green-shaded region in Fig. 2a shows the parameter range in the $\alpha$ versus $\mu$ plane where the ODE kinetics has limit cycle oscillations when $\zeta = 0.15$. In the un-shaded region, the unique steady-state for the ODE (2.24) is linearly stable and no oscillations can occur. The boundary of this region is the Hopf bifurcation curve given by $\alpha_c = \alpha_c(\mu)$ from (2.25). In Fig. 2b we plot the Hopf bifurcation boundaries for an isolated cell for four values of the efflux parameter $d_2$. We observe, as expected, that as $d_2$ increases the region where the steady-state is unstable shifts towards increasing values of the local intracellular production rate $\mu$ in (2.23).

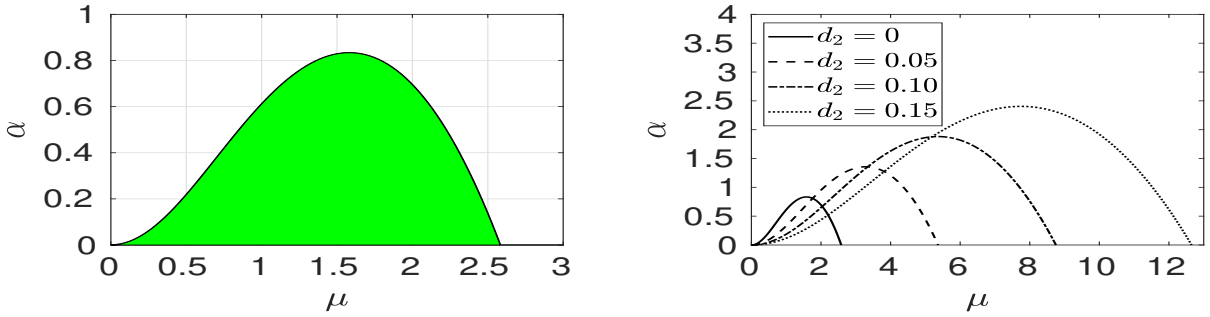


*(a) Instability region of steady-state: isolated cell* *(b) HB boundaries: isolated cell with efflux*

*Figure 2: Left: Green-shaded region where limit cycle oscillations occur for the ODE dynamics (2.24) with Sel'kov kinetics (2.23) for an uncoupled cell with no efflux, $d_2 = 0$, and with $\zeta = 0.15$. In this region, the unique steady-state of (2.24) is unstable. The Hopf bifurcation (HB) boundary is given by $\alpha_c = \alpha_c(\mu)$ in (2.25) with $d_2 = 0$. In the un-shaded region the steady-state is linearly stable. Right: HB boundaries for an isolated cell, obtained from $\alpha_c = \alpha_c(\mu)$ in (2.25) with $\zeta = 0.15$, $\tau = 0.5$, and for four values of the boundary efflux parameter $d_2$.*

Next, we examine the steady-states and their linear stability properties when the two cells are diffusively coupled through the bulk medium. Since the Green's matrix $\mathcal{G}$ is symmetric and cyclic, it follows that the NAS (2.8) has a

unique solution that is symmetric, i.e. $A_j = A_c$, $v_j = v_c$, and $w_j = w_c$, for $j = 1, 2$. From (2.8) and (2.7) we calculate

$$\begin{aligned} &v_c = \mu + \frac{2\pi D}{\tau} A_c\,, \quad w_c = \frac{\mu}{\alpha + v_c^2}\,, \\ &A_c = -\frac{\nu d_2 \mu}{d_1}\left[1 + \frac{\nu D}{d_1} + \frac{2\pi\nu D d_2}{\tau d_1} + \nu\left(\log\left(2\sqrt{D}\right) - \gamma_e + K_0\left(2/\sqrt{D}\right)\right)\right]^{-1}\,, \quad \text{where} \quad \nu \equiv \frac{-1}{\log\varepsilon}\,. \end{aligned} \tag{2.26}$$

To determine the linear stability of this symmetric steady-state we analyze the GCEP (2.20). This GCEP can be simplified owing to the fact that $J_c \equiv J_1 = J_2$, so that $\mathcal{K}$ is a multiple of the identity, i.e. $\mathcal{K} = K_c I$, where $K_c = \boldsymbol{e}_1^T(\lambda I - J_c)^{-1}\boldsymbol{e}_1$. For Sel'kov kinetics (2.23), we calculate that $K_c = K_c(\lambda)$ where

$$K_c \equiv \frac{\lambda + \det(J_c)}{\lambda^2 - \mathrm{tr}(J_c)\lambda + \det(J_c)}\,, \quad \det(J_c) = \zeta\left(\alpha + v_c^2\right)\,, \quad \mathrm{tr}(J_c) = \frac{\left[2\mu v_c - \left(\alpha + v_c^2\right) - \zeta\left(\alpha + v_c^2\right)^2\right]}{\alpha + v_c^2}\,. \tag{2.27}$$

Here $v_c$, which depends on $D$, $\tau$, $\varepsilon$, and the permeabilities $d_1$ and $d_2$, is given by (2.26). Since $\mathcal{G}_\lambda$ in (2.20a) is a cyclic symmetric matrix it has eigenvalues $R_\lambda \pm G_{\lambda 12}$ and two possible unstable modes $\boldsymbol{c}_\pm$ given by

$$\boldsymbol{c}_+ \equiv (1,1)^T\,, \quad \text{(in-phase)}\,; \qquad \boldsymbol{c}_- \equiv (1,-1)^T\,, \quad \text{(anti-phase)}\,. \tag{2.28}$$

By setting $\mathcal{M}\boldsymbol{c}_\pm = \boldsymbol{0}$ in (2.20), we obtain from (2.20b) that $\lambda \in \Lambda(\mathcal{M})$ if and only if $\mathcal{F}_\pm(\lambda) = 0$, where

$$\mathcal{F}_\pm(\lambda) \equiv 1 + \frac{D\nu}{d_1} + \frac{2\pi\nu D d_2}{\tau d_1} K_c(\lambda) + \nu\left[\log 2 - \gamma_e - \frac{1}{2}\log\left(\frac{1+\tau\lambda}{D}\right) \pm K_0\left(2\sqrt{\frac{1+\tau\lambda}{D}}\right)\right]\,. \tag{2.29}$$

In (2.29), the $+$ and $-$ signs correspond to the in-phase and anti-phase modes in (2.28), respectively. Oscillatory instabilities associated with these modes for which $\mathrm{Re}(\lambda) > 0$ and $\mathrm{Im}(\lambda) \neq 0$ yield, from (2.22), either in-phase or anti-phase small amplitude intracellular oscillations near the symmetric steady-state solution.

In our numerical computations in §3 we will choose Sel'kov kinetic parameters $\alpha$, $\mu$, and $\zeta$ for which an isolated cell only has a linearly stable steady-state solution. Our goal is to determine regions in the $(D, \tau)$ parameter plane, for fixed $d_1$ and $d_2$, where either in-phase or anti-phase intracellular oscillations occur as a result of the diffusive coupling of the two cells through the bulk medium.

# 3 Numerical Results: Two Cells in $\mathbb{R}^2$

To determine the Hopf bifurcation boundaries in the $(D, \tau)$ plane for the in-phase and anti-phase modes, we simply set $\mathcal{F}_\pm(i\lambda_I) = 0$ in (2.29). By using Newton's method and arclength continuation TEST_CON (cf. [1]) with respect to $D$, we determine the Hopf threshold and corresponding frequency $\lambda_I$ by numerically solving coupled system

$$\mathrm{Re}\left(\mathcal{F}_\pm(i\lambda_I)\right) = 0\,, \qquad \mathrm{Im}\left(\mathcal{F}_\pm(i\lambda_I)\right) = 0\,. \tag{3.1}$$

To determine regions of instability in open sets of the $\tau$ versus $D$ parameter plane we can use the winding number criterion of complex analysis to identify the number $\mathcal{N}_\pm$ of eigenvalues $\lambda \in \Lambda(\mathcal{M})$ with $\mathrm{Re}(\lambda) > 0$ for either the in-phase $(+)$ or anti-phase $(-)$ modes. By using the argument principle, the number $\mathcal{N}_\pm$ of roots of $\mathcal{F}_\pm(\lambda) = 0$ in $\mathrm{Re}(\lambda) > 0$ is $\mathcal{N} = \frac{1}{2\pi}[\arg\mathcal{F}_\pm]_\Gamma + P$, where $P$ is the number of poles of $\mathcal{F}_\pm(\lambda)$ in $\mathrm{Re}(\lambda) > 0$. Here the square brackets denotes the change in the argument of $\mathcal{F}_\pm$ over the contour $\Gamma$. The closed contour $\Gamma$ is the limit as $\rho \to \infty$ of the union of the imaginary axis, which can be decomposed as $\Gamma_{I+} = i\lambda_I$ and $\Gamma_{I-} = -i\lambda_I$, for $0 < \lambda_I < \rho$, for which $[\arg\mathcal{F}_\pm]_{\Gamma_{I+}} = [\arg\mathcal{F}_\pm]_{\Gamma_{I-}}$, and the semi-circle $\Gamma_\rho$, defined by $|\lambda| = \rho$ with $|\arg(\lambda)| \leq \pi/2$. By letting $\rho \to \infty$, we calculate from (2.29), upon using the fact that $K_0(z) \to 0$ exponentially for $|\arg z| < \pi/2$, that $[\arg\mathcal{F}_\pm]_{\Gamma_\rho} = 0$. Moreover, since $\det(J_c) > 0$ (see (2.27)), we observe from (2.29) and (2.27) that $\mathcal{F}_\pm(\lambda)$ can have two poles in $\mathrm{Re}(\lambda) > 0$ depending on the sign of $\mathrm{tr}(J_c)$, which does not depend on the mode. In this way, we obtain that the number of unstable eigenvalues $\mathcal{N}$ of the linearization around the symmetric steady-state for the two-cell problem is

$$\mathcal{N} = \mathcal{N}_+ + \mathcal{N}_-\,, \qquad \mathcal{N}_\pm = \frac{1}{\pi}[\arg\mathcal{F}_\pm]_{\Gamma_{I+}} + P\,, \qquad P = \begin{cases} 2\,, & \text{if } \mathrm{tr}(J_c) > 0\,, \\ 0\,, & \text{if } \mathrm{tr}(J_c) < 0\,. \end{cases} \tag{3.2}$$

The advantage of using (3.2) to determine $\mathcal{N}$ is that we only need do a line-sweep down the positive imaginary axis $\lambda = i\lambda_I$, with $\lambda_I > 0$, of the spectral plane, while using the winding number algorithm of [3] to calculate $[\arg \mathcal{F}_{\pm}]_{\Gamma_{I_+}}$.

In Fig. 3 we plot the Hopf bifurcation (HB) boundaries in the $\tau$ versus $D$ plane, as numerically-computed from (3.1), for the parameter set

$$\alpha = 0.9\,, \qquad \mu = 2\,, \qquad \zeta = 0.15\,, \qquad d_1 = 0.8\,, \qquad d_2 = 0.2\,, \qquad \varepsilon = 0.05\,. \tag{3.3}$$

For these Sel'kov kinetic parameters the two cells, when uncoupled from the bulk medium, only have a stable steady-state (see Fig. 2). From Fig. 3a, we observe that both the in-phase and anti-phase instability lobes are unbounded in $D$. In Fig. 3b we show results computed from the winding number criterion (3.2) for the number $\mathcal{N}$ of unstable eigenvalues of the linearization at discrete points in $(D, \tau)$ phase diagram, in which we pixelated the $\tau$ and $D$ axes into 50 equal subdivisions. In contrast to the finite-domain case in the unit disk studied in [19], where the anti-phase instability lobe is always very small, we observe from Fig. 3 that there is a large region in the parameter space where both anti-phase and in-phase oscillations can occur. Moreover, from Fig. 3b, we observe that in the upper thin magenta-shaded region in the $(D, \tau)$ parameter plane, with $D$ small enough, only unstable anti-phase intracellular oscillations can occur. In terms of the dimensional bulk diffusivity $D_B$, this region where anti-phase oscillations is dominant exists only if $D_B$ is small enough (see (1.4)). Similarly, from Fig. 3b, there is a thin (lower magenta-shaded) region in the $(D, \tau)$ parameter plane where only unstable in-phase intracellular oscillations can occur. However, when $D$ is large, i.e. for large $D_B$, we observe from Fig. 3a that the in-phase and anti-phase HB boundaries nearly coincide.

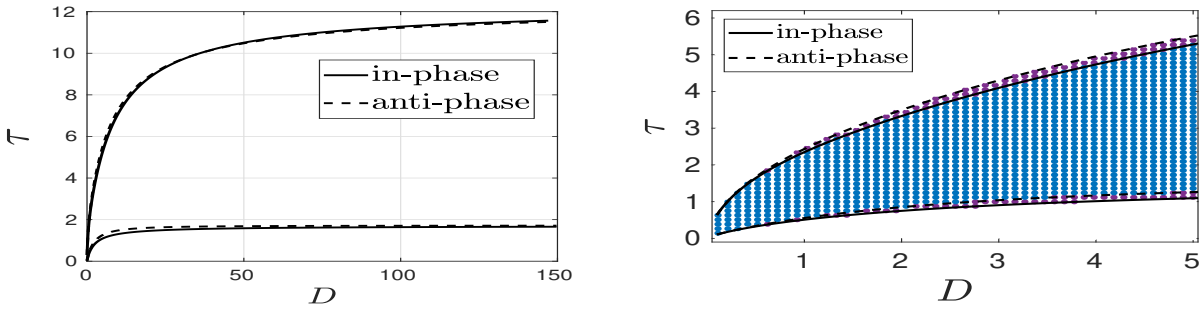


*(a) HB boundaries for two identical cells*

*(b) Number of unstable eigenvalues of the GCEP*

*Figure 3: Left: HB boundaries in the $\tau$ versus D plane for two cells for the parameter set in (3.3). The heavy solid and dashed curves are for the in-phase and anti-phase modes, respectively, as computed from the zeroes of $\mathcal{F}_{\pm}(i\lambda_I) = 0$ in (2.29). Each mode is linearly unstable within the boundaries of the curves. Right: Zoomed plot for small D of instability regions and the number $\mathcal{N}$ of unstable eigenvalues in $Re(\lambda) > 0$ given by the union of the roots of $\mathcal{F}_{\pm}(\lambda) = 0$, as computed numerically from the winding number criterion (3.2). Blue region: $\mathcal{N} = 4$. Magenta region: $\mathcal{N} = 2$. White Region: $\mathcal{N} = 0$. The HB boundaries for the in-phase and anti-phase modes are superimposed.*

In Fig. 4 we plot the real and imaginary part of the eigenvalue $\lambda$ with the largest part for both the in-phase and anti-phase modes along the vertical slice $D = 3$ through the phase diagram in Fig. 3b, as computed numerically from setting $\mathcal{F}_{\pm}(\lambda) = 0$ in (2.29). On this slice, we observe from Fig. 4a that there is a range of $\tau$ where the anti-phase and in-phase instabilities have comparable growth rates. However, as seen from Fig. 4b, the frequency of intracellular oscillations is rather insensitive to $\tau$. For four values of $\tau$, we compute from (2.29) that

$$\tau = 5.5\,; \quad \lambda = -0.01098 + i(0.8296)\,, \quad \text{(in-phase)}\,; \quad \lambda = -0.00919 + i(0.8316)\,, \quad \text{(anti-phase)}\,, \tag{3.4a}$$

$$\tau = 2.5\,; \quad \lambda = 0.02008 + i(0.7990)\,, \quad \text{(in-phase)}\,; \quad \lambda = 0.020187 + i(0.8083)\,, \quad \text{(anti-phase)}\,, \tag{3.4b}$$

$$\tau = 1.5\,; \quad \lambda = 0.03154 + i(0.7722)\,, \quad \text{(in-phase)}\,; \quad \lambda = 0.024932 + i(0.7890)\,, \quad \text{(anti-phase)}\,, \tag{3.4c}$$

$$\tau = 0.5\,; \quad \lambda = -0.1844 + i(0.7099)\,, \quad \text{(in-phase)}\,; \quad \lambda = -0.2404 + i(0.7274)\,, \quad \text{(anti-phase)}\,. \tag{3.4d}$$

Next, we illustrate these theoretical predictions from our linear stability theory by using FlexPDE [11] to numerically compute solutions to the cell-bulk PDE-ODE model (1.3), with parameters as in (3.3). In our computation we

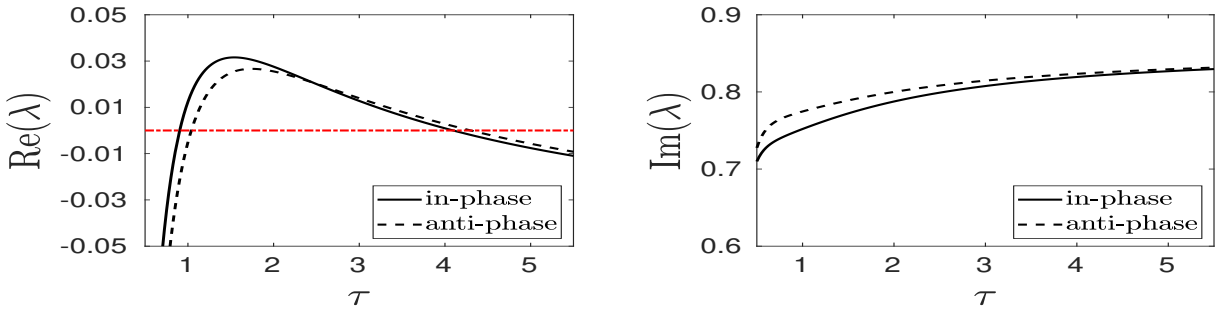


*(a) $Re(\lambda)$ versus $\tau$*

*(b) $Im(\lambda)$ versus $\tau$*

*Figure 4: Roots of (2.29) with the largest real part as a function of $\tau$ for both the in-phase and anti-phase modes along the vertical slice $D = 3$ through the HB diagram in Fig. 3b for the parameters in (3.3). Left: $Re(\lambda)$ versus $\tau$. Right: $Im(\lambda)$ versus $\tau$. We observe that there is a range of $\tau$ where both the in-phase and anti-phase modes have comparable growth rates. However, the frequency of oscillations, as determined by $Im(\lambda)$, does not depend strongly on $\tau$. The crossing $Re(\lambda) = 0$ (horizontal dashed-dotted red line) corresponds to the HB boundaries in Fig. 3b on the slice $D = 3$.*

truncated the infinite domain $\mathbb{R}^2$ to the large disk $|\boldsymbol{x}| = r \le R_M$, while imposing the artificial boundary condition

$$Du_r = -\left(\sqrt{D} + \frac{D}{2r}\right) u\,, \qquad \text{on} \quad r = R_M\,, \tag{3.5}$$

so as to minimize the reflection of diffusive waves generated by the two cells back into the domain. The precise form for this artificial boundary condition is chosen so that, upon using the well-known asymptotics $K_0(z) \sim bz^{-1/2}e^{-z}$ as $z \to \infty$, the steady state outer solution for $r \gg 1$, as given by $u \sim cK_0(r/\sqrt{D})$ for some $c$, satisfies (3.5) when $r \gg 1$. For each of the four values of $\tau$ in (3.4), and with $D = 3$ and $R_M = 15$, in Fig. 5 we show FlexPDE [11] results of (1.3) for the intracellular components $u_1$ and $u_2$ versus time and for the bulk solution at $t = 300$ (zoomed near the two cells). For $\tau = 5.5$ (top row of Fig. 5), we observe that intracellular oscillations slowly decay towards the steady-state. This slow decay is consistent with the eigenvalue result in (3.4a), where $\mathrm{Re}(\lambda) < 0$ but with $|\mathrm{Re}(\lambda)|$ very small for both modes. In contrast, when $\tau = 0.5$ (bottom row of Fig. 5), we observe a rather fast and nearly monotonic approach to the steady-state for the intracellular components. This is consistent with the eigenvalue result in (3.4d), where $|\mathrm{Re}(\lambda)|$ is no longer small. For $\tau = 1.5$, where the steady-state is unstable, (3.4c) shows that the growth rate for in-phase intracellular oscillations is larger than that for anti-phase oscillations. From the full numerical results given in the third row of Fig. 5 we observe sustained in-phase intracellular oscillations over long time scales. In contrast, when $\tau = 2.5$, in the second row of Fig. 5 we observe mixed-mode intracellular oscillations. Such oscillations are consistent with the linear stability prediction in (3.4b) in which the growth rate for the in-phase and anti-phase modes are comparable. Although our theoretical predictions are only based on a linear stability analysis of the steady-state, we conclude that they do qualitatively predict the behavior for the intracellular dynamics in the fully nonlinear regime, as observed in the numerical results shown in Fig. 5.

## 3.1 Dependence on Inter-Cell Distance

In Fig. 3 we plotted the HB boundaries in the $(D, \tau)$ plane for a fixed $d_1$, $d_2$, and $\varepsilon$. From the scaling (1.4), and since $\varepsilon = R_0/L$, Fig. 3 is useful for characterizing intracellular oscillations as the dimensional reaction rate $k_R$ and the bulk diffusivity $D_B$ are varied. However, to illustrate how the HB boundaries depend on the inter-cell distance $2L$ and $k_R$, for a fixed $D_B$, it is convenient to non-dimensionalize (1.1) by using the diffusion length $L_B$, defined by

$$L_B \equiv \sqrt{\frac{D_B}{k_B}}\,, \tag{3.6}$$

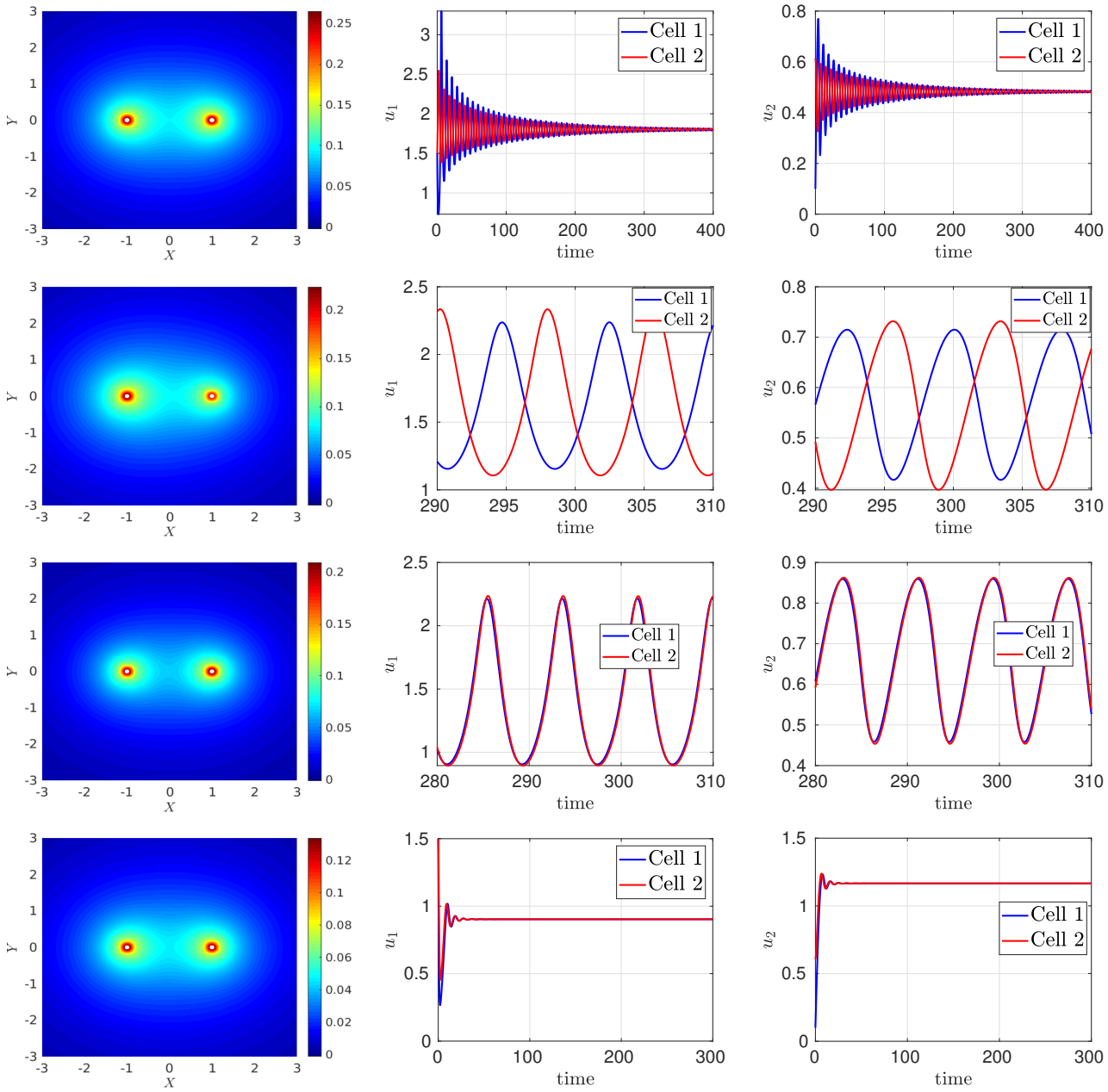


*Figure 5: Numerical results for the full PDE-ODE model (1.3) from Flexpde [11] with $D = 3$ at four values of $\tau$ for the parameters in (3.3). First column: Surface plot of the bulk solution $U$ at time $t = 300$. Second column: intracellular component $u_1$ versus $t$ for $j = 1, 2$ Third column: intracellular component $u_2$ versus $t$ for $j = 1, 2$. First row: $\tau = 5.5$. Slowly decaying intracellular oscillations lead to the steady-state. Second row: $\tau = 2.5$. Sustained mixed-mode intracellular oscillations. Third row: $\tau = 1.5$. Sustained in-phase intracellular oscillations. Fourth row: $\tau = 0.5$. Nearly monotonic approach to the steady-state.*

as the dimensional length scale. With this choice, in place of (1.3) we obtain that

$$\begin{aligned} &\tau\, U_t = \Delta U - U\,, \qquad t>0\,, \quad \boldsymbol{x}\in\mathbb{R}^2\setminus\cup_{j=1}^2\Omega_{\tilde{\varepsilon}_j}\,;\\ &\tilde{\varepsilon}\,\partial_n U = \tilde{d}_1\, U - \tilde{d}_2\, u_j^1\,, \qquad \boldsymbol{x}\in\partial\Omega_{\tilde{\varepsilon}_j}\,, \quad j=1,2\,, \end{aligned} \tag{3.7a}$$

in the bulk region, where $\Omega_{\tilde{\varepsilon}_j}\equiv\{\boldsymbol{x}\,|\,|\boldsymbol{x}-\boldsymbol{x}_j|\le\tilde{\varepsilon}\}$, $\boldsymbol{x}_1\equiv(L/L_B,0)^T$, and $\boldsymbol{x}_2\equiv(-L/L_B,0)^T$. This PDE is coupled to the common intracellular dynamics within the two cells by

$$\frac{\mathrm{d}\boldsymbol{u}_j}{\mathrm{d}t} = \boldsymbol{F}(\boldsymbol{u}_j) + \frac{\boldsymbol{e}_1}{\tilde{\varepsilon}\,\tau}\int_{\partial\Omega_{\tilde{\varepsilon}_j}}\left(\tilde{d}_1\, U - \tilde{d}_2\, u_j^1\right)\,\mathrm{d}S_{\boldsymbol{x}}\,, \qquad j=1,2\,. \tag{3.7b}$$

The dimensionless parameters in (3.7), which are all independent of $L$, are

$$\tau\equiv\frac{k_R}{k_B}\,, \qquad \tilde{\varepsilon}\equiv\frac{R_0}{L_B}\ll 1\,, \qquad \tilde{d}_1\equiv\frac{\beta_{10}}{L_B\,k_B}=\mathcal{O}(1)\,, \qquad \tilde{d}_2\equiv\frac{\beta_{20}L_B}{k_B}=\mathcal{O}(1)\,, \tag{3.8}$$

where $\beta_{10}\equiv\beta_1\tilde{\varepsilon}$ and $\beta_{20}\equiv\beta_2\tilde{\varepsilon}$.

For Sel'kov reaction kinetics, we can repeat the steady-state and linear stability analysis of §2 for (3.7) in the limit $\tilde{\varepsilon}\ll 1$. In place of (2.26) we obtain

$$v_c=\mu+\frac{2\pi}{\tau}A_c\,, \quad w_c=\frac{\mu}{\alpha+v_c^2}\,, \quad A_c=-\frac{\nu\tilde{d}_2\mu}{\tilde{d}_1}\left[1+\frac{\nu}{\tilde{d}_1}+\frac{2\pi\nu\tilde{d}_2}{\tau\tilde{d}_1}+\nu\left(\log 2-\gamma_e+K_0\left(\frac{2L}{L_B}\right)\right)\right]^{-1}\,, \tag{3.9}$$

where $K_0(z)$ is the modified Bessel function of the second kind of order zero. Moreover, in place of (2.29) we obtain that the discrete eigenvalues of the linearization around the steady-state for the in-phase and anti-phase modes are roots of $\mathcal{H}_\pm(\lambda)=0$, where

$$\mathcal{H}_\pm(\lambda)\equiv 1+\frac{\nu}{\tilde{d}_1}+\frac{2\pi\nu\tilde{d}_2}{\tau\tilde{d}_1}K_c(\lambda)+\nu\left[\log 2-\gamma_e-\frac{1}{2}\log\left(1+\tau\lambda\right)\pm K_0\left(\frac{2L}{L_B}\sqrt{1+\tau\lambda}\right)\right]\,, \tag{3.10}$$

and $\gamma_e$ is Euler's constant. Here $K_c$ is defined in (2.27) in terms of the modified $v_c$ and $w_c$ as given in (3.9).

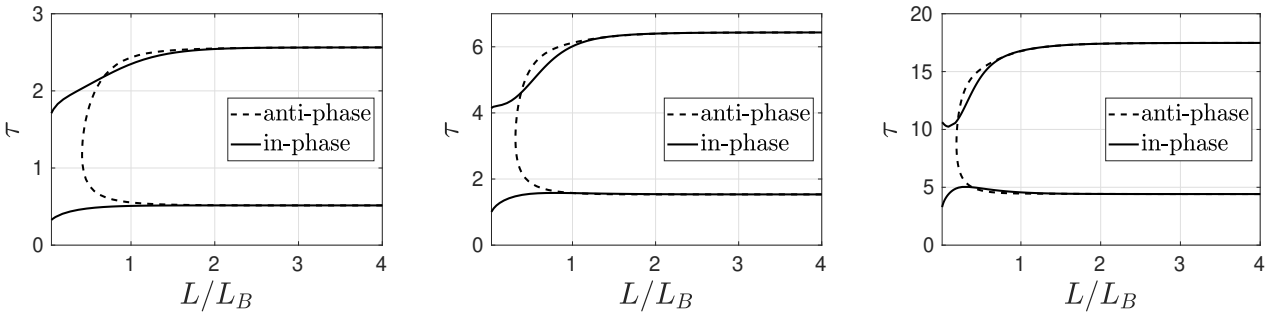


(a) $\tilde{d}_1=0.8$, $\tilde{d}_2=0.2$ (b) $\tilde{d}_1=0.4$, $\tilde{d}_2=0.4$ (c) $\tilde{d}_1=0.2$, $\tilde{d}_2=0.8$

*Figure 6: HB boundaries for the in-phase and anti-phase modes in the $\tau$ versus $L/L_B$ plane for two cells with common Sel'kov parameters $\alpha=0.9$, $\mu=2$, $\zeta=0.15$. The in-phase mode is unstable to oscillations between the solid curves. The anti-phase mode is unstable in the sideways U-shaped regions bounded by the dashed curves. Left: $\tilde{d}_1=0.8$, $\tilde{d}_2=0.2$, and $\tilde{\varepsilon}=0.05$. Middle: $D_B$ is increased by a factor of 4 so that $\tilde{d}_1=0.4$, $\tilde{d}_2=0.4$, and $\tilde{\varepsilon}=0.025$. Right: $D_B$ is now increased by a factor of 16 so that $\tilde{d}_1=0.2$, $\tilde{d}_2=0.8$, and $\tilde{\varepsilon}=0.0125$.*

In Fig. 6a we plot the anti-phase and in-phase HB boundaries in the $(L/L_B,\tau)$ parameter plane, as obtained by setting $\mathcal{H}_\pm(i\lambda_I)=0$ in (3.10), for the Sel'kov parameter set $\alpha=0.9$, $\mu=2$, $\zeta=0.15$, and with $\tilde{d}_1=0.8$, $\tilde{d}_2=0.2$, and

$\tilde{\varepsilon} = 0.05$. Two key qualitative features are observed from this figure. Firstly, anti-phase oscillations, resulting from a weak cell-to-cell communication, do not occur when $L/L_B$ is too small. As a result, as expected intuitively, in-phase synchrony through the diffusive medium is the only possible oscillatory instability when the inter-cell separation $L$ is below a threshold. The second feature is that oscillatory instabilities can occur for any inter-cellular separation, provided that the rate, $k_R$, of intracellular reactions, which determines $\tau = k_R/k_B$, is within some range.

In Fig. 6b and Fig. 6c we show how the HB boundaries in Fig. 6a are altered when the dimensional bulk diffusivity $D_B$ is increased by a factor of 4 and then by a factor of 16, respectively, from the value, labeled by $D_{B0}$, used in Fig. 6a. For these values, we obtain from (3.6) and (3.8) that the diffusion length $L_B$ increases by a factor of two or four, while $\tilde{\varepsilon}$ decreases by the same factors. The corresponding values of $\tilde{d}_1$ and $\tilde{d}_2$, obtained from (3.8), are given in the caption of Fig. 6. As $D_B$ is increased, the minimum values of $\tau$ at which in-phase intracellular oscillations occur, which are given by the lower solid curves in Fig. 6a–Fig. 6c, also increases. This implies that a larger bulk diffusivity can simply wash out the bulk signal on the unbounded domain, and not trigger oscillations, unless the intracellular reaction rate $k_R$ also increases. Moreover, we observe from the upper edge of the instability range in Fig. 6a–Fig. 6c that intracellular oscillations will occur for much larger values of $\tau$ as $D_B$ is increased.

From Fig. 6a, the minimum value of $L$ for the anti-phase HB boundary is $L = 0.4158 L_{B0}$, where $L_{B0} \equiv \sqrt{D_{B0}/k_B}$. Then, when $D_B$ is increased by a factor of 4, this minimum value is shifted to $L = 0.3135 L_B = 0.6270 L_{B0}$ since $L_B = 2L_{B0}$. When $D_B$ is increased by a factor of 16, we have $L = 0.1921 L_B = 0.7684 L_{B0}$. By comparing these values, we conclude that the minimum value of $L$ at which anti-phase intracellular oscillations occur increases as the bulk diffusion increases. When $D_B$ is increased, the signaling molecule can more readily diffuse between the two cells. As a result, when $D_B$ is large, larger inter-cellular distances are needed to ensure a weak inter-cell interaction where anti-phase oscillations are possible.

# 4 Hexagonal Arrangement of Cells in $\mathbb{R}^2$

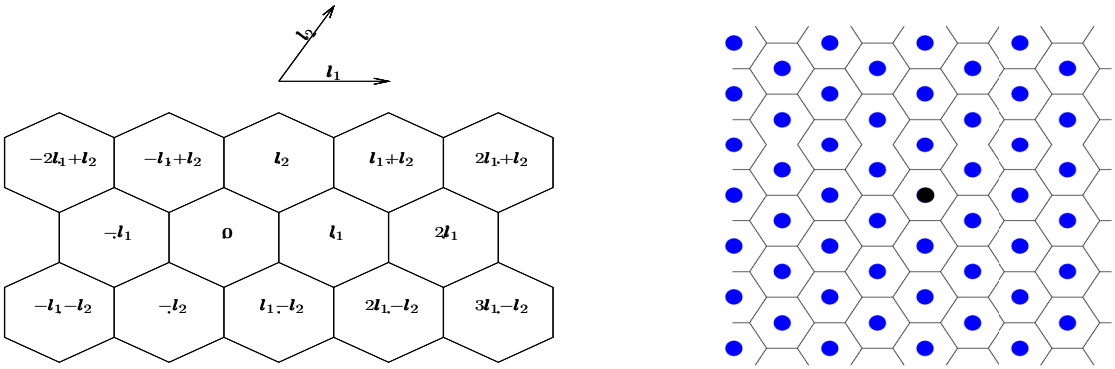


*Figure 7: Left figure: part of an infinite regular hexagonal lattice. The centers of the small compartments are labeled at the centers of the hexagons. The fundamental Wigner-Seitz (FWS) cell $\Omega$ is the regular hexagon centered at the origin $\mathbf{0}$. Right panel: the small cells of radius $\varepsilon$ (blue) for the periodic extension of the FWS cell (black) centered at the origin.*

In this section we extend the analysis in §2, which was based on the dimensionless formulation (1.3), to the case of a hexagonal arrangement of identical cells of radius $\varepsilon$ in $\mathbb{R}^2$ centered at the lattice points, given by

$$\Lambda \equiv \left\{ m\boldsymbol{l}_1 + n\boldsymbol{l}_2 \,\middle|\, m,\, n \in \mathbb{Z} \right\}, \qquad \text{where} \quad \boldsymbol{l}_1 = \left( \left(\frac{4}{3}\right)^{1/4}, 0 \right)^T, \qquad \boldsymbol{l}_2 = \left(\frac{4}{3}\right)^{1/4} \left( \frac{1}{2}, \frac{\sqrt{3}}{2} \right)^T, \tag{4.1}$$

where $\mathbb{Z}$ denotes the set of integers (see the left panel of Fig. 7). This choice of lattice vectors $\boldsymbol{l}_1$ and $\boldsymbol{l}_2$ has fixed the area of the primitive cell to unity. The *Wigner-Seitz (WS)* cell centered at a given lattice point of $\Lambda$ consists of all

points in the plane that are closer to this point than to any other lattice point, while the fundamental WS cell $\Omega$ is the one centered at the origin (see the right panel of Fig. 7). A WS cell is a convex polygon that has the same unit area $|\boldsymbol{l}_1 \times \boldsymbol{l}_2|$ of the primitive cell, and the union of these WS cells tile all of $\mathbb{R}^2$ in the sense that $\mathbb{R}^2 = \bigcup_{z\in\Lambda}(z+\Omega)$. In Fig. 7 we show this fundamental WS cell and the centers of the cells for the regular hexagonal lattice. We remark that our choice that has fixed $|\Omega| = 1$ for the non-dimensional system (1.3) implicitly defines the length scale $L$ in (1.2) for the dimensional problem (1.1).

Following [6], the reciprocal, or dual, lattice $\Lambda^\star$ is defined in terms of reciprocal vectors $\boldsymbol{d}_1$ and $\boldsymbol{d}_2$ by

$$\Lambda^\star = \left\{ m\boldsymbol{d}_1 + n\boldsymbol{d}_2 \,\middle|\, m,\, n \in \mathbb{Z} \right\}, \qquad \text{where} \quad \boldsymbol{d}_1 = \left(\frac{4}{3}\right)^{-1/4} \left(1, -\frac{1}{\sqrt{3}}\right)^T, \qquad \boldsymbol{d}_2 = \left(\frac{4}{3}\right)^{-1/4} \left(0, \frac{2}{\sqrt{3}}\right)^T, \tag{4.2}$$

which satisfy $\boldsymbol{d}_i \cdot \boldsymbol{l}_j = \delta_{ij}$ where $\delta_{ij}$ is the Kronecker symbol. The first Brillouin zone, labeled by $\Omega_b$, is defined as the Wigner-Seitz cell centered at the origin in the reciprocal space (cf. [6]). We remark that an alternative commonly used definition of the reciprocal lattice is $\Lambda^\star = \{2\pi m\,\boldsymbol{d}_1, 2\pi n\,\boldsymbol{d}_2\}_{m,n\in\mathbb{Z}}$ (cf. [21], [23]). However, our specific choice in (4.2), is motivated by the form of the Poisson summation formula of [6] given in (A.2) below, which we use to develop a computationally tractable formula for certain Green's function defined on the lattice.

To construct the steady-state solution for the cell-bulk PDE system (1.3) for the Sel'kov kinetics (2.23) in the limit $\varepsilon \to 0$ with cells centered at the lattice points, we need only construct the steady-state solution in the fundamental Wigner Seitz cell $\Omega$ and extend the solution to $\mathbb{R}^2$ using periodicity. To do so, we introduce the periodic reduced-wave Green's function $G_p(\boldsymbol{x})$ with regular part $R_p$, as defined by

$$\Delta G_p - \frac{1}{D} G_p = -\delta(\boldsymbol{x})\,; \qquad G_p(\boldsymbol{x}+\boldsymbol{l}) = G_p(\boldsymbol{x})\,, \quad \text{for} \quad \boldsymbol{l} \in \Lambda\,; \qquad R_p \equiv \lim_{\boldsymbol{x}\to\boldsymbol{0}} \left( G_p(\boldsymbol{x}) + \frac{1}{2\pi}\log|\boldsymbol{x}| \right). \tag{4.3}$$

As shown in §2 of [18], and summarized in Appendix B, the periodicity condition in (4.3) on the lattice directly implies a periodicity condition for $G_p$ on $\partial\Omega$.

The asymptotic construction of the steady-state solution for (1.3) in $\Omega$ for a single cell of radius $\varepsilon \ll 1$ centered at the origin, and with Sel'kov reaction kinetics, proceeds as in §2.1. In place of (2.26), we readily calculate in $\Omega$ that

$$v_c = \mu + \frac{2\pi D}{\tau} A_c\,, \qquad w_c = \frac{\mu}{\alpha + v_c^2}\,, \qquad A_c = -\frac{\nu d_2 \mu}{d_1}\left[1 + \frac{\nu D}{d_1} + \frac{2\pi\nu D d_2}{\tau d_1} + 2\pi\nu R_p\right]^{-1}. \tag{4.4}$$

An explicit computationally tractable expression for the regular part $R_p$ in (4.3) is given below by (4.8).

## 4.1 The linear stability problem

To analyze the linear stability of the periodic steady-state solution on the lattice we linearize (1.3) around this steady state and, by using the Floquet-Bloch theorem (cf. [20]), we need only impose a Floquet boundary condition for the eigenfunction of the linearization on $\partial\Omega$. In place of (2.29), we readily derive for $\varepsilon \to 0$ that the band $\lambda(\boldsymbol{k})$ of spectra are determined by the root of $\mathcal{F}_b(\lambda) = 0$, defined by

$$\mathcal{F}_b(\lambda) = 1 + \frac{D\nu}{d_1} + \frac{2\pi\nu D d_2}{\tau d_1} K_c(\lambda) + 2\pi\nu R_b(\boldsymbol{k}; 1+\tau\lambda)\,, \tag{4.5}$$

where $K_c(\lambda)$ is defined in (2.27) in terms of $v_c$ and $w_c$ as given in (4.4). In (4.5), $R_b(\boldsymbol{k}; z)$, with $z \equiv 1 + \tau\lambda$, is the regular part of the reduced-wave Bloch Green's function, defined for $\mathrm{Re}(z) > 0$ by

$$\Delta G_b - \frac{z}{D} G_b = -\delta(\mathbf{x})\,; \qquad G_b(\mathbf{x}+\boldsymbol{l}) = e^{-i\boldsymbol{k}\cdot\boldsymbol{l}}\, G_b(\mathbf{x})\,, \quad \boldsymbol{l} \in \Lambda\,; \qquad R_b(\boldsymbol{k}; z) \equiv \lim_{\mathbf{x}\to\boldsymbol{0}} \left( G_b(\mathbf{x}) + \frac{1}{2\pi}\log|\mathbf{x}| \right), \tag{4.6}$$

where $\boldsymbol{k}/(2\pi) \in \Omega_b$, $\Lambda$ is the hexagonal lattice in (4.1), and $\Omega_b$ is the first Brillouin zone in the reciprocal space.

The key to implementing the steady-state and linear stability theory is to determine an explicit expression for $R_b(\boldsymbol{k}; z)$, as defined by (4.6) for arbitrary $z$ with $\mathrm{Re}(z) > 0$. In Appendix A we extend the analysis in §5.1 of [17]

where, for the case $z = 1$, an Ewald summation technique was used to determine a rapidly converging expression for $R_b(\boldsymbol{k}; 1)$ in terms of infinite sums over the direct lattice $\Lambda$ of (4.1) and the reciprocal lattice $\Lambda^\star$, as defined in (4.2).

As derived in Appendix A, we have for $\mathrm{Re}(z) > 0$ that

$$R_b(\boldsymbol{k}; z) = \frac{1}{2\pi}\left(\log\left(2\sqrt{D}\right) - \gamma_e - \log(\sqrt{z})\right) - \frac{1}{4\pi} E_1\left(\frac{z}{\eta^2 D}\right) + \sum_{\substack{\boldsymbol{l}\in\Lambda \\ \boldsymbol{l}\neq\boldsymbol{0}}} e^{i\boldsymbol{k}\cdot\boldsymbol{l}}\, F_{\mathrm{sing}}(|\boldsymbol{l}|) + \sum_{\boldsymbol{d}\in\Lambda^\star} \exp\left(-\frac{|2\pi\boldsymbol{d} - \boldsymbol{k}|^2 + \frac{z}{D}}{\eta^2}\right) \frac{1}{|2\pi\boldsymbol{d} - \boldsymbol{k}|^2 + \frac{z}{D}}\,, \tag{4.7a}$$

where $\gamma_e$ is Euler's constant. Here $E_1(w) \equiv \int_1^\infty \xi^{-1} e^{-w\xi}\, d\xi$ is the exponential integral, defined for $\mathrm{Re}(w) > 0$, while $F_{\mathrm{sing}}(r)$ is defined by

$$F_{\mathrm{sing}}(r) \equiv \frac{1}{2\pi} K_0\left(r\sqrt{\frac{z}{D}}\right) - \frac{J(r;z)}{4\pi}\,, \qquad \text{where} \qquad J(r;z) \equiv \int_1^\infty \xi^{-1} e^{-z\xi/(\eta^2 D)} e^{-r^2\eta^2/(4\xi)}\, d\xi\,. \tag{4.7b}$$

In (4.7), $\eta > 0$ is the user-defined Ewald cut-off parameter chosen so that both infinite lattice sums in (4.7a) converge rapidly. Finally, in (4.4), we identify that

$$R_p = R_b(\boldsymbol{0}; 1)\,. \tag{4.8}$$

## 4.2 Numerical Results

We first use Newton's method on (4.5) to compute the curves in the $\tau$ versus $D$ plane where $\lambda = i\lambda_I$ is a root of

$$\mathrm{Re}\left(\mathcal{F}_b(i\lambda_I)\right) = 0\,, \qquad \mathrm{Im}\left(\mathcal{F}_b(i\lambda_I)\right) = 0\,, \tag{4.9}$$

for the in-phase synchronous mode where $\boldsymbol{k} = \boldsymbol{0}$. To numerically compute $R_b(\boldsymbol{0}; z)$ and $R_p \equiv R_b(\boldsymbol{0}; 1)$ from (4.7), we introduce subsets $\bar{\Lambda}$ and $\bar{\Lambda}^\star$ of the direct and reciprocal lattices $\Lambda$ and $\Lambda^\star$, respectively, defined in terms of $M_1 > 0$ and $M_2 > 0$ by

$$\bar{\Lambda} \equiv \left\{n_1\boldsymbol{l}_1 + n_2\boldsymbol{l}_2 \,\middle|\, -M_1 < n_1, n_2 < M_1\right\}\,, \quad \bar{\Lambda}^\star \equiv \left\{n_1\boldsymbol{d}_1 + n_2\boldsymbol{d}_2 \,\middle|\, -M_2 < n_1, n_2 < M_2\right\}\,, \quad n_1, n_2 \in \mathbb{Z}\,. \tag{4.10}$$

To numerically evaluate the complex-valued integral $J$ in (4.7b) we used a Gauss-Laguerre quadrature with $N_q = 200$ nodes after first separating $J$ into real and imaginary parts. In addition, we used standard algorithms to compute the exponential integral $E_1(w)$ and $K_0(w)$ of a complex argument. In our computations, the Ewald cut-off parameter was taken as $\eta = 2$, while $M_1$ and $M_2$ were chosen so that the absolute value of the increment obtained by increasing $M_1$ and $M_2$ by one in the two lattice sums in (4.7a) are each less than $10^{-6}$. In implementing this convergence criteria for the infinite lattice sums, we typically obtained $M_1 = 7$ and $M_2 = 4$ for the results shown in Fig. 8.

In Fig. 8 we plot the boundaries in the $\tau$ versus $D$ plane where $\lambda = i\lambda_I$ for the in-phase synchronous mode $\boldsymbol{k} = \boldsymbol{0}$ for three values of the cell influx parameter $d_1$. The other parameters, chosen to be the same as for the two-cell case studied in §3, are

$$\alpha = 0.9\,, \qquad \mu = 2\,, \qquad \zeta = 0.15\,, \qquad d_2 = 0.2\,, \qquad \varepsilon = 0.05\,. \tag{4.11}$$

By using a numerical winding number computation on (4.5) for $\boldsymbol{k} = \boldsymbol{0}$, we conclude that the in-phase mode is unstable only within the lobes shown in Fig. 8. In contrast to the two-cell case (see Fig. 3), we observe that there is much narrower range of $\tau$ where in-phase oscillations can occur for the periodic problem. As $d_1$ decreases, leading to a reduction of the influx of the bulk signal into the cells, we observe from Fig. 8 that the in-phase instability lobe becomes bounded. When the lobe is closed, no in-phase oscillations can occur when the bulk diffusivity is too large.

Next, we provide an analytical confirmation of the results shown in Fig. 8 for large $D$. For $D \gg 1$, we obtain

$$R_b(\boldsymbol{0}; 1 + \tau\lambda) \sim \frac{D}{1 + \tau\lambda} + R_{p0} + o(1)\,, \tag{4.12}$$

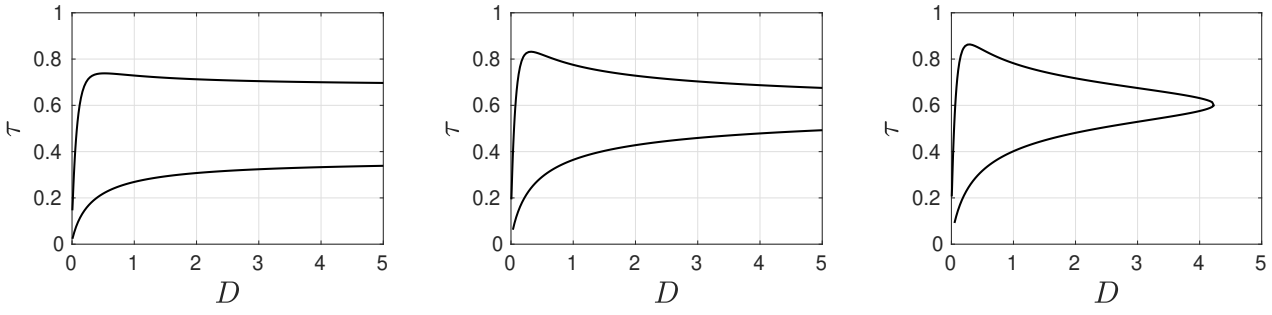


(a) $d_1 = 0.8$ (b) $d_1 = 0.6$ (c) $d_1 = 0.55$

*Figure 8: Plot of the boundaries in the $\tau$ versus $D$ plane where $\lambda = i\lambda_I$ is a root of $\mathcal{F}_b(i\lambda_I) = 0$ in (4.9) for the in-phase mode $\boldsymbol{k} = \boldsymbol{0}$ for three values of the influx parameter $d_1$ when the efflux is $d_2 = 0.2$. Parameters: $\zeta = 0.15$, $\mu = 2$, $\alpha = 0.9$, and cell radius $\varepsilon = 0.05$. As $d_1$ decreases, the interval in $\tau$ where the in-phase mode is unstable first shrinks and then pinches off at some finite $D$ when $d_1$ is on the range $0.55 < d_1 < 0.6$.*

from Appendix B, here $R_{p0} \approx -0.21027$ is the regular part of the periodic source-neutral Green's function defined by the PDE (B.6). This yields that $R_p = R_b(\boldsymbol{0}; 1) \approx D + R_{p0}$ for $D \gg 1$. Then, upon substituting (4.12) into (4.5), we obtain after some lengthy but straightforward algebra, that when $\boldsymbol{k} = \boldsymbol{0}$ and $D \gg 1$, $\lambda$ is a root of the cubic

$$\lambda^3 + q_1\lambda^2 + q_2\lambda + q_3 = 0\,, \tag{4.13a}$$

where the coefficients $q_1$, $q_2$, and $q_3$ are given by

$$q_1 \equiv \frac{\gamma_2}{\gamma_1\tau} + \frac{1}{\gamma_1} - \mathrm{tr}(J_c)\,, \qquad q_2 \equiv \left(1 + \frac{1}{\gamma_1}\right)\det(J_c) + \frac{1}{\gamma_1\tau} - \frac{\gamma_2}{\gamma_1\tau}\mathrm{tr}(J_c)\,, \qquad q_3 \equiv \frac{(1+\gamma_2)}{\gamma_1\tau}\det(J_c)\,, \tag{4.13b}$$

in terms of $\gamma_1$ and $\gamma_2$ defined by

$$\gamma_1 \equiv \frac{\tau}{2\pi d_2}\left(1 + \frac{d_1}{D\nu} + \frac{2\pi d_1 R_{p0}}{D}\right)\,, \qquad \gamma_2 \equiv \gamma_1 + \frac{d_1\tau}{d_2}\,. \tag{4.13c}$$

Since $\det(J_c) > 0$, we have $q_3 > 0$. As a result, by the Routh-Hurwitz criterion, the roots of (4.13a) satisfy $\mathrm{Re}(\lambda) < 0$ if and only if $q_1 > 0$ and $q_1q_2 - q_3 > 0$. Moreover, (4.13) has a complex conjugate pair $\lambda = \pm i\lambda_I$, with an additional real eigenvalue $\lambda < 0$, when

$$q_1 > 0 \quad \text{and} \quad q_1q_2 - q_3 = 0\,. \tag{4.14}$$

For the values of $d_1$ in Fig. 8, in the left and right panels of Fig. 9 we plot $q_1q_2 - q_3$ and $q_1$ versus $\tau$, respectively, for the parameters in (4.11) on the vertical slice $D = 5$ through the phase diagrams in Fig. 8. From Fig. 9 we observe that there are two values $\tau_{H\pm}$ of $\tau$ where (4.14) is satisfied when $d_1 = 0.8$ and $d_1 = 0.6$. When $d_1 = 0.8$, we compute $\tau_{H-} \approx 0.338$ and $\tau_{H+} \approx 0.697$, while when $d_1 = 0.6$, we get $\tau_{H-} \approx 0.492$ and $\tau_{H+} \approx 0.675$. These critical values, obtained from the analysis of a cubic, are very close to the threshold values of $\tau$ in the left and middle panels of Fig. 8 when $D = 5$. In contrast, when $d_1 = 0.55$, we observe from Fig. 9 that $q_1q_2 - q_3 > 0$ and $q_1 > 0$, which establishes that all the roots to (4.13a) satisfy $\mathrm{Re}(\lambda) < 0$ when $D = 5$. This latter prediction from the large $D$ theory agrees with the results shown in the right panel of Fig. 8.

Our results so far for the periodic problem have been restricted to the consideration of in-phase instabilities where $\boldsymbol{k} = \boldsymbol{0}$. However, since the spectrum of the linearization is not discrete, we must seek conditions on the parameters that ensure that the *entire band* of spectra, written as $\lambda(\boldsymbol{k})$, satisfies $\mathrm{Re}(\lambda(\boldsymbol{k})) < 0$ *for all* $\boldsymbol{k}/2\pi \in \Omega_b$. This issue is explored numerically by using Newton's method to solve (4.5) for $\lambda(\boldsymbol{k})$ using the explicit formula for $R_b(\boldsymbol{k}; 1 + \tau\lambda)$ in (4.7). In Fig. 10a we plot $\mathrm{Im}(\lambda(\boldsymbol{k}))$ versus $\mathrm{Re}(\lambda(\boldsymbol{k}))$ for $D = 5$ for the two threshold values of $\tau$ in Fig. 8a at which the in-phase mode $\boldsymbol{k} = \boldsymbol{0}$ satisfies $\mathrm{Re}(\lambda(\boldsymbol{0})) = 0$. From this figure we observe that at the lower threshold value of $\tau$ we have that the entire spectral band satisfies $\mathrm{Re}(\lambda(\boldsymbol{k})) < 0$ for $\boldsymbol{k} \neq 0$. As a result, for these parameter values,

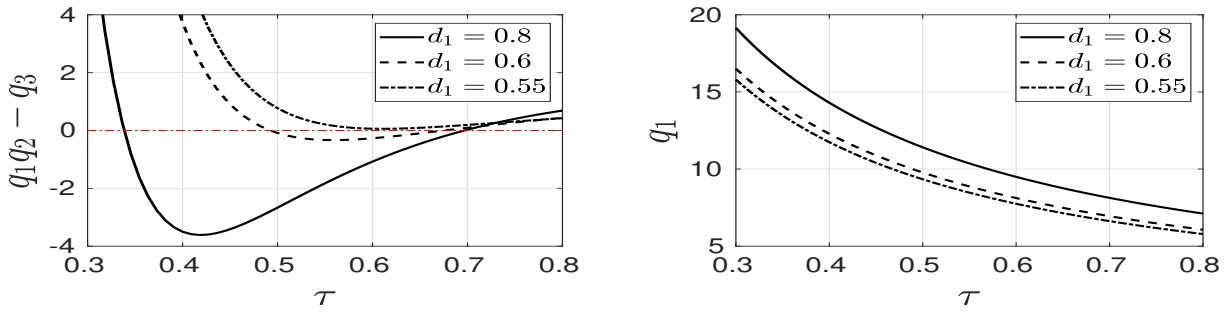


*(a)* $q_1q_2 - q_3$ *versus* $\tau$ *(b)* $q_1$ *versus* $\tau$

*Figure 9: Plots of* $q_1q_2 - q_3$ *(left panel) and* $q_1$ *(right panel) versus* $\tau$ *for the three values of* $d_1$ *in Fig. 8 when* $D = 5$ *for the parameters in (4.11). Since* $q_1 > 0$*, from the Routh Hurwitz criteria (4.14), the cubic (4.13a) has pure imaginary roots* $\lambda = \pm i\lambda_I$ *at values of* $\tau$ *when* $q_1q_2 - q_3 = 0$ *(horizontal red line) and* $Re(\lambda) > 0$ *when* $q_1q_2 - q_3 < 0$*.*

the lower stability threshold is indeed set by the in-phase mode $\boldsymbol{k} = \mathbf{0}$. However, we observe from Fig. 10a that at the upper threshold value of $\tau$, a portion of the band $\lambda(\boldsymbol{k})$ already lies in the unstable half-plane $\mathrm{Re}(\lambda) > 0$. As a consequence, the upper stability threshold is not determined by the in-phase mode $\boldsymbol{k} = \mathbf{0}$. In Fig. 10b and Fig. 10c we show similar results for vertical slices through Fig. 8a at two smaller values of $D$. These spectral results are qualitatively analogous to those obtained in §3 for the two-cell problem, where from Fig. 3b we recall that the lower threshold value of $\tau$ is set by the in-phase mode while the upper threshold is set by the anti-phase mode. For our periodic problem, further numerical evidence (not shown) for other parameter values in Fig. 8 lead to the conjecture that the instability threshold as $\tau$ is increased from a small value is always set by the in-phase mode. Recalling that $\tau = k_R/k_B$, the implication of this conjecture is that, for an infinite lattice of cells, in-phase synchrony of intracellular oscillations can be triggered by slowly increasing the reaction-rate $k_R$ of intracellular kinetics.

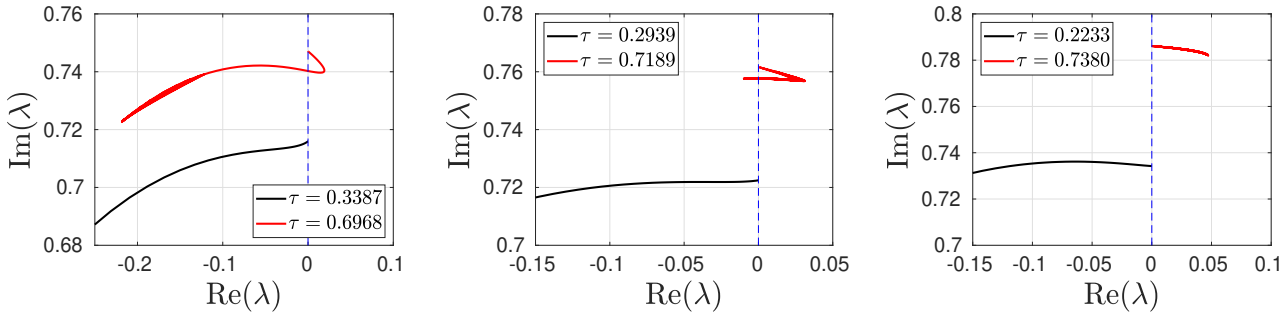


*(a)* $D = 5$ *(b)* $D = 1.52$ *(c)* $D = 0.531$

*Figure 10: Plots of the band* $\lambda(\boldsymbol{k})$ *of spectra at three values of* $D$*, as computed from (4.5) and (4.7), at the two threshold values of* $\tau$ *for which the in-phase mode* $\boldsymbol{k} = \mathbf{0}$*, with parameters as in Fig. 8a, satisfies the marginal stability condition* $Re(\lambda(\mathbf{0})) = 0$*. It is only for the lower threshold value of* $\tau$ *that the entire band* $\lambda(\boldsymbol{k})$ *satisfies* $Re(\lambda(\boldsymbol{k})) < 0$ *for* $\boldsymbol{k} \neq \mathbf{0}$*.*

# 5 Discussion

We have used the cell-bulk PDE-ODE model (1.1) to analyze the onset of diffusion-induced oscillations for two spatially segregated, but dynamically active, small cells in $\mathbb{R}^2$. By using strong localized perturbation theory in the limit of small cell radius (cf. [34], [35]), we have constructed steady-state solutions and formulated the linear stability problem for the dimensionless cell-bulk PDE-ODE model (1.3) with two identical cells on $\mathbb{R}^2$. For the specific choice

of Sel'kov intracellular reactions, we have analyzed how the coupling of dynamically active cells through diffusion of a signaling molecule in the bulk medium can lead to the triggering of in-phase or anti-phase intracellular oscillations through a Hopf bifurcation that would otherwise not occur for cells that are uncoupled from the bulk medium. Moreover, synchronous oscillatory instabilities for a hexagonal arrangement of identical cells in $\mathbb{R}^2$ was studied for Sel'kov kinetics by determining a new explicit formula for the regular part of a certain periodic reduced-wave Green's function. Our study of diffusion-induced synchrony, based on (1.3), provides an alternative theoretical framework to the more classical, but strictly ODE-based, approaches used for studying collective synchronous behavior that arises from coupling discrete dynamically active units (see [27] for a recent survey).

We now briefly discuss two extensions of this study. Firstly, our analysis of the two-cell problem is restricted to the case where the inter-cell separation is much larger than the common radii of the two cells. In this limit, where the two cells are isolated, they communicate only through diffusion in the outer bulk medium. As a result, our analysis is not applicable to characterizing intracellular oscillations of a two-cell cluster, where the inter-cell separation is comparable to the cell radius. For this more intricate case, although the outer problem, defined at $\mathcal{O}(1)$ distances from a two-cell cluster, is readily solved analytically in terms of a free-space Green's function, the challenge is with regards to calculating the inner solution for both the symmetric steady-state and linear stability problems. However, since these inner problems involve solving Laplace's equation with a Robin boundary condition outside two circular cells, it should be possible to approximate their solutions numerically by extending the simple least-squares fitting approach of [31] for solving Laplace's equation outside a collection of circular disks. In this direction, it would be worthwhile to develop and implement a hybrid asymptotic-numerical theory for characterizing the onset of intracellular oscillations from the linearization of a symmetric steady-state solution for a two-cell cluster.

A second open direction is to extend the cell-bulk model (1.1) to allow for advection of the signaling molecule in the bulk medium (cf. [33]). By including a spatially uniform drift velocity $\boldsymbol{B}$, (1.1) becomes

$$\begin{aligned} &\frac{\partial \mathcal{U}}{\partial T} = D_B\,\Delta\mathcal{U} - \boldsymbol{B}\cdot\nabla\mathcal{U} - k_B\,\mathcal{U}\,, \qquad T>0\,, \quad \boldsymbol{X}\in\mathbb{R}^2\setminus\cup_{j=1}^2\,\Omega_j\,;\\ &\qquad (D_B\,\nabla\mathcal{U} - \boldsymbol{B}\mathcal{U})\cdot\hat{\boldsymbol{n}} = \beta_1\,\mathcal{U} - \beta_2\,\mu_j^1\,, \qquad \boldsymbol{X}\in\partial\Omega_j\,, \quad j=1,2\,, \end{aligned} \tag{5.1}$$

which is coupled to the intracellular dynamics by (1.1c). In (5.1), $\hat{\boldsymbol{n}}$ is the unit outward normal to the circular cells, which points into the bulk region. By using the diffusion length $L_B\equiv\sqrt{D_B/k_B}$ to non-dimensionalize (5.1) as was done in §3.1, we obtain in place of (3.7a) that

$$\begin{aligned} &\tau\,U_t = \Delta U - \boldsymbol{b}\cdot\nabla U - U\,, \qquad t>0\,, \quad \boldsymbol{x}\in\mathbb{R}^2\setminus\cup_{j=1}^2\Omega_{\tilde{\varepsilon}_j}\,;\\ &\tilde{\varepsilon}\,(\nabla U - \boldsymbol{b}U)\cdot\hat{\boldsymbol{n}} = \tilde{d}_1\,U - \tilde{d}_2\,u_j^1\,, \qquad \boldsymbol{x}\in\partial\Omega_{\tilde{\varepsilon}_j}\,, \quad j=1,2\,, \end{aligned} \tag{5.2}$$

which is coupled to the dimensionless intracellular dynamics (3.7b). Here $\boldsymbol{b}\equiv\boldsymbol{B}/(k_BL_B)$ and the other dimensionless parameters are as in (3.8). It should be possible, by using a similar asymptotic analysis as in §2, to analyze the effect of the uniform flow $\boldsymbol{b}$ on triggering intracellular oscillations near an asymmetric steady-state solution for the two-cell configuration. Depending on the direction of the drift $\boldsymbol{b}$ the advection should either enhance or diminish the possibility of intracellular oscillations. In the steady-state and linear stability analysis for (5.2) when $\tilde{\varepsilon}\ll 1$, the Green's function $G(\boldsymbol{x};\boldsymbol{\xi})$, satisfying

$$\Delta G - \boldsymbol{b}\cdot\nabla G - cG = -\delta(\boldsymbol{x}-\boldsymbol{\xi})\,, \tag{5.3}$$

with either $c=1$ or $c=1+\tau\lambda$, will play a prominent role. It has the explicit solution

$$G(\boldsymbol{x};\boldsymbol{\xi}) = \frac{1}{2\pi}e^{\boldsymbol{b}\cdot(\boldsymbol{x}-\boldsymbol{\xi})/2}K_0\left(|\boldsymbol{x}-\boldsymbol{\xi}|\left[c+|\boldsymbol{b}|^2/4\right]^{1/2}\right)\,. \tag{5.4}$$

## Acknowledgements

Michael Ward gratefully acknowledges the financial support from the NSERC Discovery grant program.

# Appendices

## A The Quasi-Periodic Reduced-wave Green's function

We develop a rapidly converging expansion for the Bloch Green's function $G_b(\mathbf{x})$ and its regular part $R_b(\boldsymbol{k};z)$ as defined by (4.6). To do so, we extend the analysis in §5.1 of [17] for the case $z=1$, as was motivated by the methodology in [6], to allow for complex-valued $z$ with $\mathrm{Re}(z)>0$. Then, by setting $z=1+\tau\lambda$ we obtain $R_b(\boldsymbol{k};1+\tau\lambda)$, as needed in (4.5). Moreover, we identify that $R_p \equiv R_b(\mathbf{0};1)$ in (4.3) and (4.4).

We begin by representing the solution to (4.6) as the sum of free-space Green's functions

$$G_b(\mathbf{x}) = \sum_{\boldsymbol{l}\in\Lambda} G_{\text{free}}(\mathbf{x}+\boldsymbol{l})\, e^{i\boldsymbol{k}\cdot\boldsymbol{l}}\,, \tag{A.1}$$

which ensures that the quasi-periodicity condition in (4.6) is satisfied. Then, to analyze (A.1) we use the Poisson summation formula which converts a sum over the hexagonal lattice $\Lambda$ to a sum over the reciprocal lattice $\Lambda^\star$ of (4.2). In the notation of [6], we have (see Proposition 2.1 of [6])

$$\sum_{\boldsymbol{l}\in\Lambda} f(\mathbf{x}+\boldsymbol{l})\, e^{i\boldsymbol{k}\cdot\boldsymbol{l}} = \frac{1}{|\Omega|}\sum_{\boldsymbol{d}\in\Lambda^\star} \hat{f}(2\pi\boldsymbol{d}-\boldsymbol{k})\, e^{i\mathbf{x}\cdot(2\pi\boldsymbol{d}-\boldsymbol{k})}\,, \quad \mathbf{x},\boldsymbol{k}\in\mathbb{R}^2\,. \tag{A.2}$$

Here $|\Omega|$ is the area of the primitive cell of the lattice, while $\hat{f}$ is the Fourier transform of $f$, defined in $\mathbb{R}^2$ by

$$\hat{f}(\boldsymbol{p}) \equiv \int_{\mathbb{R}^2} f(\mathbf{x})\, e^{-i\mathbf{x}\cdot\boldsymbol{p}}\,\mathrm{d}\mathbf{x}\,, \qquad f(\mathbf{x}) = \frac{1}{4\pi^2}\int_{\mathbb{R}^2} \hat{f}(\boldsymbol{p})\, e^{i\boldsymbol{p}\cdot\mathbf{x}}\,\mathrm{d}\boldsymbol{p}\,. \tag{A.3}$$

Upon applying (A.2) to (A.1) we obtain that the sum over the reciprocal lattice consists of free-space Green's functions in the Fourier domain. By taking the Fourier transform of the PDE $\Delta G_{\text{free}} - zD^{-1}G_{\text{free}} = -\delta(\mathbf{x})$ for the free-space Green's function, we obtain that $\hat{G}_{\text{free}}(\boldsymbol{p}) = \hat{G}_{\text{free}}(|\boldsymbol{p}|)$, where

$$\hat{G}_{\text{free}}(\rho) = \frac{1}{\rho^2+\frac{z}{D}}\,, \qquad \text{with} \quad \rho\equiv|\boldsymbol{p}|\,. \tag{A.4}$$

Then, from (A.2) and (A.1), and by using $|\Omega|=1$, we obtain that

$$G_b(\mathbf{x}) = \frac{1}{|\Omega|}\sum_{\boldsymbol{d}\in\Lambda^\star} \hat{G}_{\text{free}}(2\pi\boldsymbol{d}-\boldsymbol{k})\, e^{i\mathbf{x}\cdot(2\pi\boldsymbol{d}-\boldsymbol{k})} = \sum_{\boldsymbol{d}\in\Lambda^\star} \frac{e^{i\mathbf{x}\cdot(2\pi\boldsymbol{d}-\boldsymbol{k})}}{|2\pi\boldsymbol{d}-\boldsymbol{k}|^2+\frac{z}{D}}\,. \tag{A.5}$$

In order to obtain a rapidly converging infinite series representation for $G_b(\mathbf{x})$, we introduce the decomposition

$$\hat{G}_{\text{free}}(2\pi\boldsymbol{d}-\boldsymbol{k}) = \alpha(2\pi\boldsymbol{d}-\boldsymbol{k},\eta)\,\hat{G}_{\text{free}}(2\pi\boldsymbol{d}-\boldsymbol{k}) + \Big(1-\alpha(2\pi\boldsymbol{d}-\boldsymbol{k},\eta)\Big)\,\hat{G}_{\text{free}}(2\pi\boldsymbol{d}-\boldsymbol{k})\,, \tag{A.6}$$

where the function $\alpha(2\pi\boldsymbol{d}-\boldsymbol{k},\eta)$ is defined by

$$\alpha(2\pi\boldsymbol{d}-\boldsymbol{k},\eta) = \exp\left(-\frac{|2\pi\boldsymbol{d}-\boldsymbol{k}|^2+\frac{z}{D}}{\eta^2}\right)\,. \tag{A.7}$$

Here $\eta>0$ is a real-valued cutoff parameter, which is specified below. Since $\mathrm{Re}(z)>0$, we readily calculate that

$$\lim_{\eta\to 0}\alpha(2\pi\boldsymbol{d}-\boldsymbol{k},\eta)=0\,; \qquad \lim_{\eta\to\infty}\alpha(2\pi\boldsymbol{d}-\boldsymbol{k},\eta)=1\,.$$

With this choice for $\alpha$, the sum over $\boldsymbol{d}\in\Lambda^\star$ in (A.5) of the first set of terms in (A.6), as labeled by

$$G_{\text{fourier}}(\mathbf{x}) \equiv \sum_{\boldsymbol{d}\in\Lambda^\star} \exp\left(-\frac{|2\pi\boldsymbol{d}-\boldsymbol{k}|^2+\frac{z}{D}}{\eta^2}\right)\,\frac{e^{i\mathbf{x}\cdot(2\pi\boldsymbol{d}-\boldsymbol{k})}}{|2\pi\boldsymbol{d}-\boldsymbol{k}|^2+\frac{z}{D}}\,, \tag{A.8}$$

converges absolutely when $\mathrm{Re}(z) > 0$.

Next, we calculate the lattice sum in (A.5) over the second set of terms in (A.6) by using the inverse transform (A.3) after first writing $(1-\alpha)\,\hat{G}_{\rm free}$ as an integral. To do so, we define $\rho \equiv |2\pi\boldsymbol{d} - \boldsymbol{k}|$, so that from (A.7) and (A.4)

$$(1-\alpha(2\pi\boldsymbol{d}-\boldsymbol{k},\eta))\;\hat{G}_{\rm free}(2\pi\boldsymbol{d}-\boldsymbol{k}) = \frac{1}{\rho^2+\frac{z}{D}}\left(1-\exp\left(-\frac{\rho^2+\frac{z}{D}}{\eta^2}\right)\right) = \hat{\chi}(\rho) \equiv \int_{\log\eta}^{\infty} 2\,e^{-\left(\rho^2+\frac{z}{D}\right)e^{-2s}-2s}\,ds\,. \quad \text{(A.9)}$$

In recognizing the middle term in (A.9) as the integral $\hat{\chi}(\rho)$ we used the easily verified definite integral

$$2\int_{\log\eta}^{\infty} e^{-(\rho^2+\frac{z}{D})e^{-2s}-2s}\,ds = \frac{e^{-(\rho^2+\frac{z}{D})e^{-2s}}}{\rho^2+\frac{z}{D}}\Big|_{s=\log\eta}^{s=\infty} = \frac{1}{\rho^2+\frac{z}{D}}\left(1-\exp\left(-\frac{\rho^2+\frac{z}{D}}{\eta^2}\right)\right)\,. \quad \text{(A.10)}$$

Next, we take the inverse Fourier transform of (A.9). To do so, we use two key facts. Firstly, the inverse Fourier transform of a radially symmetric function $\hat{f}(\rho)$ is the inverse Hankel transform of order zero (cf. [25]), so that $f(r) = (2\pi)^{-1}\int_0^\infty \hat{f}(\rho)\,J_0(\rho r)\,\rho\,d\rho$. Secondly, from [25], we recall the well-known inverse Hankel transform

$$\int_0^\infty e^{-\rho^2\,e^{-2s}}\,\rho\,J_0(\rho r)\,d\rho = \frac{1}{2}\,e^{2s-r^2\,e^{2s}/4}\,.$$

In this way, we calculate using the definition of $\hat{\chi}(\rho)$ in (A.9) that

$$\begin{aligned}\chi(r) \equiv \frac{1}{2\pi}\int_0^\infty \hat{\chi}(\rho)\,J_0(\rho r)\,\rho\,d\rho &= \frac{1}{\pi}\int_{\log\eta}^{\infty} e^{-2s-ze^{-2s}/D}\left(\int_0^\infty e^{-\rho^2 e^{-2s}}\,\rho\,J_0(\rho r)\,d\rho\right)ds \\ &= \frac{1}{2\pi}\int_{\log\eta}^{\infty} e^{-2s-ze^{-2s}/D}\,e^{2s-\frac{r^2}{4}e^{2s}}\,ds = \frac{1}{2\pi}\int_{\log\eta}^{\infty} e^{-\left(\frac{r^2}{4}e^{2s}+\frac{z}{D}e^{-2s}\right)}\,ds\,.\end{aligned}$$

In the notation of [6], we then define $F_{\rm sing}(|\mathbf{x}|)$ as

$$F_{\rm sing}(|\mathbf{x}|) \equiv \frac{1}{2\pi}\int_{\log\eta}^{\infty} e^{-\left(\frac{|\mathbf{x}|^2}{4}e^{2s}+\frac{z}{D}e^{-2s}\right)}\,ds\,. \quad \text{(A.11)}$$

Therefore, by using the Poisson summation formula (A.2) to calculate lattice sum in (A.5) over the second set of terms in (A.6), we obtain

$$G_{\rm spatial}(\mathbf{x}) \equiv F_{\rm sing}(|\mathbf{x}|) + \sum_{\substack{\boldsymbol{l}\in\Lambda\\ \boldsymbol{l}\neq\mathbf{0}}} e^{i\boldsymbol{k}\cdot\boldsymbol{l}}\,F_{\rm sing}(|\mathbf{x}+\boldsymbol{l}|)\,. \quad \text{(A.12)}$$

In summary, the Bloch Green's function for the reduced-wave operator in the spatial domain, satisfying (4.6), is $G_b(\mathbf{x}) = G_{\rm fourier}(\mathbf{x}) + G_{\rm spatial}(\mathbf{x})$, representing the sum of (A.8) and (A.12). In this way, we have

$$G_b(\mathbf{x}) = \sum_{\boldsymbol{d}\in\Lambda^\star} \frac{e^{-\frac{|2\pi\boldsymbol{d}-\boldsymbol{k}|^2+\frac{z}{D}}{\eta^2}}\;e^{i\mathbf{x}\cdot(2\pi\boldsymbol{d}-\boldsymbol{k})}}{|2\pi\boldsymbol{d}-\boldsymbol{k}|^2+\frac{z}{D}} + F_{\rm sing}(|\mathbf{x}|) + \sum_{\substack{\boldsymbol{l}\in\Lambda\\ \boldsymbol{l}\neq\mathbf{0}}} e^{i\boldsymbol{k}\cdot\boldsymbol{l}}\,F_{\rm sing}(|\mathbf{x}+\boldsymbol{l}|)\,, \quad \text{(A.13)}$$

where $F_{\rm sing}(|\mathbf{x}|)$ is defined in (A.11). In terms of the Ewald cut-off parameter $\eta$, we observe from (A.8) that $G_{\rm fourier}(\mathbf{x}) \to 0$ as $\eta \to 0$, while from (A.12) and (A.11) we get that $G_{\rm spatial}(\mathbf{x}) \to 0$ as $\eta \to \infty$.

The next step in the analysis is to isolate the logarithmic singularity in (A.13) as $\mathbf{x} \to \mathbf{0}$, so as to identify the regular part $R_b(\boldsymbol{k};z)$ defined by

$$R_b(\boldsymbol{k};z) \equiv \lim_{\mathbf{x}\to\mathbf{0}}\left(G_b(\mathbf{x}) + \frac{1}{2\pi}\log|\mathbf{x}|\right)\,. \quad \text{(A.14)}$$

From (A.8) we observe that $G_{\rm fourier}(\mathbf{0})$ is finite for all $|2\pi\boldsymbol{d}-\boldsymbol{k}|$ and $0<\eta<\infty$ when $\mathrm{Re}(z)>0$. Likewise, for the last set of terms in (A.13), we can take the limit $\mathbf{x}\to\mathbf{0}$ to conclude that $\sum_{\substack{\boldsymbol{l}\in\Lambda\\ \boldsymbol{l}\neq\mathbf{0}}} e^{i\boldsymbol{k}\cdot\boldsymbol{l}}\,F_{\rm sing}(|\boldsymbol{l}|)$ is also finite. As a result, the logarithmic singularity in $G_b$ as $\mathbf{x}\to 0$ must arise from the middle term, $F_{\rm sing}(r)$, in (A.13), where $r \equiv |\mathbf{x}|$.

To analyze $F_{\rm sing}(r)$ when $\mathrm{Re}(z) > 0$, we write $z = |z|e^{i\theta}$, where $\theta \equiv \mathrm{Arg} z$ satisfies $|\theta| < \pi/2$. In the integrand of (A.11) we introduce the new variable $t$ by

$$s = -\frac{1}{4}\log\left(\frac{r^2 D}{4|z|}\right) + \frac{t}{2}\,, \tag{A.15}$$

so that (A.11) becomes

$$F_{\rm sing}(r) = \frac{1}{4\pi}\int_{\beta}^{\infty} \exp\left(-r\sqrt{\frac{z}{D}}\cosh\left(t - i\theta/2\right)\right)\,dt\,, \qquad \text{where} \qquad \beta \equiv \log\left(\frac{\eta^2 r\sqrt{D}}{2\sqrt{|z|}}\right)\,. \tag{A.16}$$

Here $\theta \equiv \mathrm{Arg} z$ and we have specified the principal branch for $\sqrt{z}$. We then split the integration range in (A.16) as

$$F_{\rm sing}(r) = \frac{1}{4\pi}\int_{-\infty}^{\infty} \exp\left(-r\sqrt{\frac{z}{D}}\cosh\left(t - i\theta/2\right)\right)\,dt - \frac{1}{4\pi}\int_{-\infty}^{\beta} \exp\left(-r\sqrt{\frac{z}{D}}\cosh\left(t - i\theta/2\right)\right)\,dt\,. \tag{A.17}$$

To calculate the first term in (A.17), we use a contour integration over the box-shaped contour $-b \le \mathrm{Re}(t) \le b$ and $0 \le \mathrm{Im}(t) < \pi/2$ in the complex $t$-plane. Since there are no residues within the contour, and we have exponential decay on the sides of the box as $b \to \infty$, we can replace $t - i\theta/2$ by $t$ in (A.17) and then use symmetry to obtain

$$\frac{1}{4\pi}\int_{-\infty}^{\infty} \exp\left(-r\sqrt{\frac{z}{D}}\cosh\left(t - i\theta/2\right)\right)\,dt = \frac{1}{2\pi}\int_{0}^{\infty} \exp\left(-r\sqrt{\frac{z}{D}}\cosh\left(t\right)\right)\,dt = \frac{1}{2\pi}\int_{1}^{\infty} \frac{e^{-r\xi\sqrt{z/D}}}{\sqrt{\xi^2-1}}\,d\xi\,, \tag{A.18}$$

where the last equality in (A.18) follows from the substitution $\xi = \cosh(t)$. The last integral in (A.18) is identified by using the well-known integral representation $K_0(\omega) = \int_1^\infty e^{-\omega\xi}/\sqrt{\xi^2-1}\,d\xi$ for the modified Bessel function of the second kind of order zero, which is valid for $|\mathrm{Arg}\,\omega| < \pi/2$. In this way, we obtain from (A.18) and (A.17) that

$$F_{\rm sing}(r) = \frac{1}{2\pi}K_0\left(r\sqrt{\frac{z}{D}}\right) - \frac{J(r;z)}{4\pi}\,, \quad \text{where} \quad J(r;z) \equiv \int_{-\infty}^{\beta} \exp\left(-r\sqrt{\frac{z}{D}}\cosh\left(t - i\theta/2\right)\right)\,dt\,. \tag{A.19}$$

Next, we provide a more tractable representation for $J(r;z)$. We introduce a new variable $\xi$ defined by

$$\xi = e^{-(t-\beta)} = \frac{\eta^2 r\sqrt{D}}{2\sqrt{|z|}}e^{-t}\,, \tag{A.20}$$

so that $\xi = 1$ when $t = \beta$ and $\xi \to +\infty$ as $t \to -\infty$. In terms of $\xi$, the exponential in the integral $J$ is

$$-r\sqrt{\frac{z}{D}}\cosh\left(t - i\theta/2\right) = -\frac{z\xi}{\eta^2 D}\left(1 + \frac{\eta^4 r^2 D}{4z\xi^2}\right)\,. \tag{A.21}$$

By using (A.21) and $dt = -d\xi/\xi$ within the integral $J$ in (A.19), we obtain that (A.19) transforms to

$$F_{\rm sing}(r) = \frac{1}{2\pi}K_0\left(r\sqrt{\frac{z}{D}}\right) - \frac{J(r;z)}{4\pi}\,, \qquad \text{where} \qquad J(r;z) \equiv \int_1^\infty \frac{e^{-z\xi/(\eta^2 D)}}{\xi}e^{-r^2\eta^2/(4\xi)}\,d\xi\,. \tag{A.22}$$

Finally, we use (A.22) to extract the local behavior of $F_{\rm sing}(r)$ as $r \to 0$. As $r \to 0$, we calculate for $J(r;z)$ that

$$J \sim E_1\left(\frac{z}{\eta^2 D}\right) + \mathcal{O}(r^2)\,, \qquad \text{when} \quad \mathrm{Re}(z) > 0\,, \tag{A.23}$$

where $E_1(w) \equiv \int_1^\infty \xi^{-1}e^{-w\xi}\,d\xi$, for $\mathrm{Re}(w) > 0$, is the well-known exponential integral. In addition, in (A.22) we use $K_0(w) \sim -\log w + \log 2 - \gamma_e + o(1)$ as $|w| \to 0$, where $\gamma_e$ is Euler's constant. In this way, (A.22) and (A.23) yield

$$F_{\rm sing}(r) \sim -\frac{1}{2\pi}\log r + \frac{1}{2\pi}\left[\log(2\sqrt{D}) - \gamma_e - \log(\sqrt{z})\right] - \frac{1}{4\pi}E_1\left(\frac{z}{\eta^2 D}\right) + o(1)\,, \qquad \text{as} \quad r \to 0\,. \tag{A.24}$$

Finally, by substituting (A.13) in (A.14), and using (A.24), we obtain the result for $R_b(\boldsymbol{k};z)$ given in (4.7).

## B Formulation on the Wigner Seitz Cell

In this appendix, we provide a key result for $R_b(\boldsymbol{k};z)$. However, before doing so, we first must obtain a more refined description of the fundamental Wigner-Seitz (FWS) cell, as was discussed in §2.2 of [18]. For a general lattice, there are eight nearest neighbor lattice points to $\mathbf{x}=0$ given by the set

$$P \equiv \{\, m\boldsymbol{l}_1 + n\boldsymbol{l}_2 \,|\, m\in\{0,1,-1\}\,,\ n\in\{0,1,-1\}\,,\ \ (m,n)\neq 0\}\,. \tag{B.1}$$

For each (vector) point $\boldsymbol{P}_i \in P$, for $i=1,\ldots,8$, the Bragg line $L_i$ is defined as the line that crosses the point $\boldsymbol{P}_i/2$ orthogonally to $\boldsymbol{P}_i$. The unit outer normal to $L_i$ is labeled by $\boldsymbol{\eta}_i \equiv \boldsymbol{P}_i/|\boldsymbol{P}_i|$. The convex hull generated by these Bragg lines is the FWS cell $\Omega$. Specifically, for the hexagonal lattice (4.1) its boundary $\partial\Omega$ is the union of exactly six Bragg lines, and the centers of the Bragg lines generating $\partial\Omega$ are re-indexed as $\boldsymbol{P}_i/2$ for $i=1,\ldots,6$. The boundary $\partial\Omega$ of $\Omega$ is the union of the re-indexed Bragg lines $L_i$ for $i=1,\ldots,6$, and is parameterized segment-wise as

$$\partial\Omega = \Big\{ \mathbf{x}\in \bigcup_i \{\frac{\boldsymbol{P}_i}{2} + t\boldsymbol{\eta}_i^{\perp}\} \ \Big|\ \ -t_i \le t \le t_i\,,\ \ i=1,\ldots,6 \Big\}\,, \tag{B.2}$$

where $2t_i$ is the length of $L_i$. Here $\boldsymbol{\eta}_i^{\perp}$ is the direction perpendicular to $\boldsymbol{P}_i$, and is, therefore, tangent to $L_i$. From this construction, Bragg lines on $\partial\Omega$ must come in pairs. In particular, if $\boldsymbol{P}$ is a neighbor of 0 and the Bragg line crossing $\boldsymbol{P}/2$ lies on $\partial\Omega$, it follows by symmetry that the Bragg line crossing $-\boldsymbol{P}/2$ must also lie on $\partial\Omega$.

Next, we reformulate the PDE (4.6) for the reduced-wave Bloch Green's function $G_b$ on $\mathbb{R}^2$ to an equivalent PDE on the FWS $\Omega$. This is done by imposing a boundary operator $\mathcal{P}_k$ on $\partial\Omega$ that incorporates the quasi-periodic condition in (4.6). This equivalent PDE is

$$\Delta G_b - \frac{z}{D}G_b = -\delta(\mathbf{x})\,,\quad \mathbf{x}\in\Omega\,; \qquad \mathcal{P}_k G_b = 0\,,\quad \mathbf{x}\in\partial\Omega\,; \qquad R_b(\boldsymbol{k};z) \equiv \lim_{\mathbf{x}\to\mathbf{0}}\left( G_b(\mathbf{x}) + \frac{1}{2\pi}\log|\mathbf{x}| \right)\,, \tag{B.3}$$

where $\boldsymbol{k}/(2\pi)\in\Omega_b$. In (B.3), the boundary operator is defined by

$$\mathcal{P}_k G_b \equiv \Big\{ G_b \,\Big|\, \begin{pmatrix} G_b(\mathbf{x}_{i1}) \\ \partial_n G_b(\mathbf{x}_{i1}) \end{pmatrix} = e^{-i\boldsymbol{k}\cdot\boldsymbol{l}_i} \begin{pmatrix} G_b(\mathbf{x}_{i2}) \\ \partial_n G_b(\mathbf{x}_{i2}) \end{pmatrix}\,,\quad \forall\,\mathbf{x}_{i1}\in L_i\,,\ \forall\,\mathbf{x}_{i2}\in L_{-i}\,,\ \boldsymbol{l}_i\in\Lambda\,,\ \ i=1,\ldots,3 \Big\}\,. \tag{B.4}$$

Here $L_i$ and $L_{-i}$ denote two parallel Bragg lines on opposite sides of $\partial\Omega$ for $i=1,\ldots,3$, while $\mathbf{x}_{i1}\in L_i$ and $\mathbf{x}_{i2}\in L_{-i}$ are any two opposing points on these Bragg lines. In this notation, periodic boundary conditions refer to $\mathcal{P}_0 G_b = 0$.

With this reformulation of (4.6) to the PDE (B.3) on the FWS cell $\Omega$, with unit area $|\Omega|=1$, we now derive a result is needed in §4.2. Firstly, we obtain for the periodic problem, with $\mathcal{P}_0 G_b = 0$ on $\partial\Omega$, that $G_b = \mathcal{O}(D)$ when $D\gg 1$. By expanding in powers of $D$, we readily derive for $\boldsymbol{k}=\mathbf{0}$ that

$$G_b \sim \frac{D}{1+\tau\lambda} + G_{p0} + \mathcal{O}(D^{-1})\,, \tag{B.5}$$

where $G_{p0}(\mathbf{x})$ is the periodic source-neutral Green's function satisfying

$$\Delta G_{p0} = \frac{1}{|\Omega|} - \delta(\mathbf{x})\,,\quad \mathbf{x}\in\Omega\,; \qquad \mathcal{P}_0 G_{p0} = 0\,,\quad \mathbf{x}\in\partial\Omega\,; \qquad R_{p0} \equiv \lim_{\mathbf{x}\to\mathbf{0}}\left( G_{p0}(\mathbf{x}) + \frac{1}{2\pi}\log|\mathbf{x}| \right)\,, \tag{B.6}$$

and normalized by $\int_\Omega G_{p0}\,d\mathbf{x} = 0$. From Theorem 1 of [7], $R_{p0}\approx -0.21027$ is given explicitly by

$$R_{p0} = -\frac{1}{2\pi}\ln(2\pi) - \frac{1}{2\pi}\ln\Big| \sqrt{\sin\Big(\frac{\pi}{3}\Big)}\, e^{\pi i\xi/6} \prod_{n=1}^{\infty}\big(1-e^{2\pi i n\xi}\big)^2 \Big|\,, \qquad \text{where} \qquad \xi \equiv e^{i\pi/3}\,. \tag{B.7}$$

By taking the regular part of (B.5) we obtain the two-term result for $R_b(\mathbf{0};1+\tau\lambda)$ in (4.12), which is valid for $D\gg 1$.

## References


[1] Continuation Test: a MATLAB library which defines test functions for continuation codes. http://people.math.sc.edu/Burkardt/m_src/test_con/test_con.html. Accessed: 2020-02-26.

[2] M. Abramotitz and I. Stegun. *Handbook of mathematical functions*. Dover Publications, New York, New York, 9th edition, 1965.

[3] D. Alciatore and R. Miranda. A winding number and point-in-polygon algorithm. *Glaxo Virtual Anatomy Project Research Report, Department of Mechanical Engineering, Colorado State University*, 1995.

[4] T. Betcke, N. G. Highan, V. Mehrmann, G. M. N. Porzio, C. Schröder, and Tisseur F. NLEVP: A collection of nonlinear eigenvalue problems. users' guide. *MIMS EPring 2011.117, Manchester Institue for Mathematical Sciences, The University of Manchester, UK*, page 10 pages, updated 2019.

[5] T. Betcke, N. G. Highan, V. Mehrmann, C. Schröder, and Tisseur F. NLEVP: A collection of nonlinear eigenvalue problems. *ACM Trans. Math. Software*, 39(2):7.1–7.28, 2013.

[6] G. Beylkin, C. Kurcz, and L. Monzón. Fast algorithms for Helmholtz Green's functions. *Proc. R. Soc. A*, 464:3301–3326, 2008.

[7] X. Chen and Y. Oshita. An application of the modular function in nonlocal variational problems. *Arch. Rat. Mech. Anal.*, 186(1):109–132, 2007.

[8] S. Danø, M. F. Madsen, and P. G. Sørensen. Quantitative characterization of cell synchronization in yeast. *Proceedings of the National Academy of Sciences*, 104(31):12732–12736, 2007.

[9] S. Danø, P. G. Sørensen, and F. Hynne. Sustained oscillations in living cells. *Nature*, 402(6759):320–322, 1999.

[10] S. De Monte, F. d'Ovidio, S. Danø, and P. G. Sørensen. Dynamical quorum sensing: Population density encoded in cellular dynamics. *Proceedings of the National Academy of Sciences*, 104(47):18377–18381, 2007.

[11] FlexPDE. *PDE Solutions inc*, 2015. Available at http://www.pdesolutions.com.

[12] M. Gao, H. Zheng, Y. Ren, R. Lou, F. Wu, W. Yu, X. Liu, and X. Ma. A crucial role for spatial distribution in bacterial quorum sensing. *Scientific Reports*, 6(34695), 2016.

[13] J. Gou and M. J. Ward. An asymptotic analysis of a 2-D model of dynamically active compartments coupled by bulk diffusion. *J. Nonlin. Science*, 26(4):979–1029, 2016.

[14] J. Gou and M. J. Ward. Oscillatory dynamics for a coupled membrane-bulk diffusion model with Fitzhugh-Nagumo kinetics. *SIAM J. Appl. Math.*, 76(2):776–804, 2016.

[15] T. Gregor, K. Fujimoto, N. Masaki, and S. Sawai. The onset of collective behavior in social amoebae. *Science*, 328(5981):1021–1025, 2010.

[16] S. Güttel and F. Tisseur. The nonlinear eigenvalue problem. *Acta Numerica*, 26(1):1–94, 2017.

[17] D. Iron, J. Rumsey, and M. J. Ward. A hybrid asymptotic-numerical method for stability thresholds of periodic patterns of localized spots for reaction-diffusion systems in $\mathbb{R}^2$. *Europ. J. Appl. Math.*, 26(3):325–353, 2015.

[18] D. Iron, J. Rumsey, M. J. Ward, and J. C. Wei. Logarithmic expansions and the stability of periodic patterns of localized spots for reaction-diffusion systems in $\mathbb{R}^2$. *J. Nonlin. Science*, 24(5):564–627, 2014.

[19] S. Iyaniwura and M. J. Ward. Synchrony and oscillatory dynamics for a 2-D PDE-ODE model of diffusion-sensing with small signaling compartments. *submitted, SIAM J. Appl. Dyn. Sys., (40 pages)*, 2020.

[20] P. Kuchment. *Floquet theory for partial differential equations*. Birkhauser, Basel, 1993.

[21] C. M. Linton. Lattice sums for the Helmholtz equation. *SIAM Rev.*, 52(4):630–674, 2010.

[22] M. Marenda, M. Zanardo, A. Trovato, F. Seno, and A. Squartini. Modeling quorum sensing trade-offs between bacterial cell density and system extension from open boundaries. *Scientific Reports*, 6(39142), 2016.

[23] A. Moroz. Quasi-periodic Green's functions of the Helmholtz and Laplace equations. *J. Phys. A: Math. Gen.*, 39(36):11247–11282, 2006.

[24] J. Müller, C. Kuttler, B. A. Hense, M. Rothballer, and A. Hartmann. Cell–cell communication by quorum sensing and dimension-reduction. *Journal of mathematical biology*, 53(4):672–702, 2006.

[25] R. Piessens. The Hankel transform. In A. D. Poularikas, editor, *Transforms and Applications Handbook*, chapter 9. CRC Press, Boca Raton, Florida, 3rd edition, 2018.

[26] E. E. Sel'kov. Self-oscillations in glycolysis 1. A simple kinetic model. *European Journal of Biochemistry*, 4(1):79–86, 1968.

[27] T. Stankovski, T. Pereira, P. V. E. McClintock, and A. Stefanovska. Coupling functions: Universal insights into dynamical interaction mechanisms. *Rev, Mod. Phys.*, 89:045001, 2017.

[28] A. F. Taylor, M. Tinsley, and K. Showalter. Insights into collective cell behavior from populations of coupled chemical oscillators. *Phys. Chemistry Chem Phys.*, 17(31):20047–20055, 2015.

[29] M. R. Tinsley, A. F. Taylor, Z. Huang, and K. Showalter. Emergence of collective behavior in groups of excitable catalyst-loaded particles: Spatiotemporal dynamical quorum sensing. *Phys. Rev. Lett.*, 102:158301, 2009.

[30] M. R. Tinsley, A. F. Taylor, Z. Huang, F. Wang, and K. Showalter. Dynamical quorum sensing and synchronization in collections of excitable and oscillatory catalytic particles. *Physica D*, 239(11):785–790, 2010.

[31] N. Trefethon. Series solution of Laplace problems. *ANZIAM J.*, 60:1–26, 2018.

[32] A. Trovato, F. Seno, M. Zanardo, S. Alberghini, A. Tondello, and A. Squartini. Quorum vs. diffusion sensing: A quantitative analysis of the relevance of absorbing or reflecting boundaries. *FEMS Microbiology Letters*, 352:198–203, 2014.

[33] H. Uecker, J. Müller, and B. A. Hense. Individual-based model for quorum sensing with background flow. *Bull. Math. Biol.*, 76:1727–1746, 2014.

[34] M. J Ward. Spots, traps, and patches: Asymptotic analysis of localized solutions to some linear and nonlinear diffusive systems. *Nonlinearity*, 31(8):R189, 2018.

[35] M. J. Ward, W. D. Henshaw, and J. B. Keller. Summing logarithmic expansions for singularly perturbed eigenvalue problems. *SIAM J. Appl. Math.*, 53(3):799–828, 1993.

[36] S. Y. Yamamoto, C. M. Surko, and M. B. Maple. Spatial coupling in heterogeneous catalysis. *J. Chem. Phys.*, 103(18):8209, 1995.